

Fabrication and Characterization of Nanofluidic Channels for Studying Molecular Dynamics in Confined Environments

by

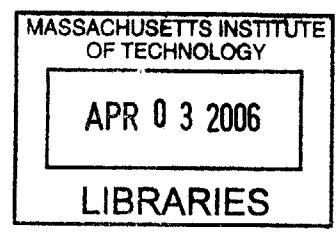
Pan Mao

B.S., Mechanical Engineering
University of Science and Technology of China, 2002

Submitted to the Department of Mechanical Engineering
in Partial Fulfillment of the Requirements for the Degree of
Master of Science in Mechanical Engineering

at the

Massachusetts Institute of Technology
February 2005

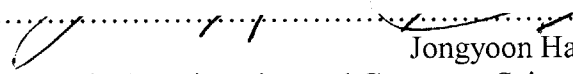


© 2005 Massachusetts Institute of Technology. All rights reserved.


Signature of Author.....

Department of Mechanical Engineering
January 15, 2005

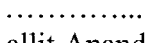
Certified by.....


Jongyoon Han
Assistant Professor of Electrical Engineering and Computer Science
Biological Engineering Division
Thesis Supervisor

Certified by.....


.....
Peter So
Associate Professor of Mechanical Engineering
Biological Engineering Division
Thesis Supervisor

Accepted by.....


.....
Lallit Anand
Professor of Mechanical Engineering
Chairman, Department Committee on Graduate Students

Fabrication and Characterization of Nanofluidic Channels for Studying Molecular Dynamics in Confined Environments

by

Pan Mao

Submitted to the Department of Mechanical Engineering in Partial Fulfillment of the Requirements for the Degree of Master of Science in Mechanical Engineering

Abstract

This thesis has characterized the applicability and limitation of PDMS micromolding and the substrate bonding techniques including both anodic (Si-glass) and thermal fusion (glass-glass) bonding, in fabricating sub-100-nm thick nanofluidic channels, which will be used for a controlled experimental study of molecular and fluidic transport in confined space. It is found that the fabrication of nanofluidic channels using PDMS substrate is generally limited to the thickness of ~100 nm because of the softness of the materials. Also, the gas permeability of PDMS poses a significant challenge in the operation of the nanofluidic devices. We demonstrate that nanofluidic channels, as thin as 20 nm with high aspect ratio (more than 250:1, width to depth) on silicon substrate and 25 nm with aspect ratio of 2000 on glass substrate can be achieved with anodic bonding technique and direct glass-glass bonding technique, respectively. Scanning electron microscopy (SEM) measurement is used to prove that the channels are of good uniformity and there is no significant change of the depth of nanofluidic channels due to anodic bonding process and glass-glass bonding process.

In addition, we have demonstrated massively-parallel vertical nanofluidic filters, with fluidic conductance as large as standard microfluidic channels, by using a combination of deep reactive ion etching (DRIE) and anisotropic KOH etching followed by an oxidation step. The lateral nanofilter array device achieved separation of the mixture of λ -DNA and Hind III digest of lambda DNA in half an hour by the mechanism of entropic trapping. The fabrication strategy for the nanofilter array device can be further optimized to achieve the uniform gap. These devices could be a key to the high-throughput nanofluidic sample-preparation microsystems.

Thesis Supervisor: Jongyoon Han

Title: Assistant Professor of Electrical Engineering and Computer Science and Biological Engineering Division

Acknowledgements

First of all, I owe numerous thanks to my advisor, Professor Jongyoon Han, for his guidance, encouragement, intellectual wisdom, and professional support during the thesis work. I truly appreciate his introducing me to this exciting research area, and have learned a great deal throughout my affiliation with him.

Many thanks to Professor Peter So for being my academic advisor and for his helpful suggestions and guidance. Also many thanks to Professor George Haller for bringing me to MIT and his kind help.

I would like to thank all of my group members, Arnaud, Chang-Soo, Jianping, Ying-Chih, Noel, Yong-Ak, for their help and friendship. I am grateful to live and work together with them. I also would like to thank my collaborators (Dr. Michael Previte, Anthony Balducci, Daeyeon Lee) for their technical support and friendship. I would like to thank my friends (Yong, Lin, Liang, Yi, Lu, Fuwan *et al.*), who have made my graduate life worthwhile. I would like to thank Cambridge Church, where I had memorable experience.

I would like to thank MIT Mechanical Engineering department (especially Ms. Leslie Regan), and Microsystems Technology Laboratories (Dr. Vicky Diadiuk, Kurt Broderick, Paul Tierney, Gwen Donahue, Brian McKenna, Bob Bicchieri). I also gratefully acknowledge financial support from MIT Lincoln Laboratory, National Science Foundation NSE, and CAREER program.

Finally, I would like to express my deepest appreciation to my grandparents and parents for their selfless love and support, and my friends in China for their lifelong friendship and support. Especially, I would like to thank my fiancée, Zhen, for her forever love and meticulous care, and for anything.

Table of Contents

List of Figures	6
List of Tables	8
Chapter 1 Introduction	9
1.1 Background	9
1.2 Fabrication of Nanofluidic Devices- Previous Works	10
1.3 Application of Nanofluidics	12
1.4 Thesis Objectives	14
1.5 Thesis Outline	14
Chapter 2 Fabrication of PDMS Nanofluidic Channels	16
2.1 Background	16
2.2 Fabrication Process	18
2.2.1 Overview of Fabrication Process	18
2.2.2 Fabrication of Silicon Masters	18
2.3 Results and Discussion	20
2.4 Conclusions	24
Chapter 3 Fabrication of Nanofluidic Channels on Silicon Substrate	26
3.1 Anodic Bonding: Applications and Mechanism	27
3.2 Fabrication Process	29
3.3 Results and Discussion	31
3.3.1 Characterization of Nanochannel Fabrication	31
3.3.2 Depth Measurement after Anodic Bonding	34
3.3.3 Limitation of Silicon-Glass Nanofluidic Channels	39
Chapter 4 Fabrication of Nanofluidic Channels on Glass Substrate	41
4.1 Glass-Glass Bonding	42

4.2 Fabrication Process	44
4.3 Results and Discussion	46
4.3.1 Characterization of Device Fabrication	46
4.3.2 Depth Measurement after Thermal Fusion Bonding	53
4.4 Conclusions	54
Chapter 5 Fabrication of Vertical Nanofluidic Channels by Anisotropic Etching of Silicon	56
5.1 Background	57
5.2 Experimental Methods	59
5.2.1 Fabrication Technique	59
5.2.2 Sample, Electrophoresis Condition, and Microscopy	63
5.3 Results and Discussion	63
5.3.1 Fabrication Characterization	63
5.3.2 Separation of Long DNA Molecules	68
5.4 Conclusions	74
Chapter 6 Summary	75
6.1 Thesis Contributions	75
6.2 Ongoing Research	76
6.3 Outlook and Future work	81
Appendices	83
Process Flow for Fabrication of PDMS Nanofluidic Channels	83
Process Flow for Fabrication of Nanofluidic Channels on Silicon Substrate	85
Process Flow for Fabrication of Nanofluidic Channels on Glass Substrate	86
References	87

List of Figures

Figure 2.1 Process of silicon masters for PDMS micromolding	19
Figure 2.2 Optical micrograph of h-PDMS nanofluidic channels with alternative thin and thick regions	21
Figure 2.3 (A) Schematic description of water plug in a PDMS channel sealed with glass substrate (side view). (B) Fluorescence image of phycoerythrin protein in a PDMS channel	23
Figure 3.1 Schematic diagram of anodic glass-silicon bonding. Control parameters are temperature, materials and bias voltage	27
Figure 3.2 Fabrication process of nanofluidic channels on silicon substrate	30
Figure 3.3 Optical observation of the survival or collapse of the channels	32
Figure 3.4 (A) Fluorescence imaging of 20 nm deep nanofluidic channels being filled with concentrated FITC dye in TBE 5X buffer solution. (B) (Bright field) microscopic image of 20 nm deep silicon nanofluidic channels spaced by 3 μm	33
Figure 3.5 Layout of the test pattern consisting of an array of 2 cm long parallel lines with various widths spaced at 5 μm from each other	36
Figure 3.6 Cross-sectional SEM images and close-up of nanochannels with the depth of 180 nm (A), 80 nm (B), 40 nm (C), and 20 nm (D) on silicon substrate (bottom wafer) bonded to a borofloat wafer (top wafer), respectively	38
Figure 4.1 Schematic of fabrication process of nanofluidic channels on glass substrate	44
Figure 4.2 The etched depth of nanofluidic channels as a function of etching time of glass without agitation in BOE (7:1) etchant	47
Figure 4.3 Optical micrograph of glass nanochannels	51
Figure 4.4 Surface profile of a glass channel etched for 30 sec in BOE (7:1) without agitation, using atomic force microscopy	52
Figure 4.5 Cross-sectional SEM images of nanochannels with the depth of 100 nm, 55 nm and 25 nm fabricated on glass substrate bonded with another glass cover	54
Figure 5.1 Alignment marks for determining the minimum underetch of the Si (111) planes	60
Figure 5.2 (A) Outline of generating lateral nanofluidic filters (top view). (B) Fabrication process of vertical nanofluidic filters with DRIE/anisotropic etching	62
Figure 5.3 Cross-sectional SEM micrograph of a trench array. Long vertical slot structures were achieved by KOH etching for 10 min	64
Figure 5.4 Cross-sectional SEM images of narrow and deep trenches after a combination of DRIE and KOH etching	66
Figure 5.5 (A) Schematic diagram of the lateral nanofilter array device. (B) Top-view schematic picture of the periodic lateral array of nanofilters with an alternative narrow region (20~200 nm) and wide region (3~4 μm)	69
Figure 5.6 (A, B, C) Sequential fluorescence images of launching DNA samples. (D) The	

cross-sectional SEM image of lateral entropic filters	70
Figure 5.7 Separation of the mixture of λ -DNA and λ -DNA digested by Hind III	72
Figure 6.1 Stochastic motion (trajectories) of molecules (red spots) in a free space (A) and in a confined 2D space (B)	78
Figure 6.2 Schematic diagram of two-photon FCS setup for the measurement of diffusion coefficient in a nanofluidic channel	79
Figure 6.3 Schematic diagram of a large DNA molecule confined to a slit channel with a depth of d	81

List of Tables

Table 2.1 Comparison of Sylgard 184 PDMS and h-PDMS 21

Table 3.1 Survival or collapse of the nanofluidic channels after anodic bonding 31

Table 3.2 Comparison of nanochannel depths before bonding and after bonding 37

Table 4.1 Survival or collapse of the nanochannels consisting of 2 cm long parallel lines
spaced by 5 μm after direct glass-glass bonding 49

Chapter 1 Introduction

1.1 Background

Microfluidics has gained tremendous success over the past decade in areas including microelectronics, analytical chemistry, drug discovery, genomics, proteomics and tissue engineering as well as other biological applications. A number of review papers for a wide range of its applications can be found¹⁻⁷. Microfluidic devices offer the advantages, as compared to traditional technologies, including huge decrease in reagent consumption, lower cost, smaller overall size, faster processes, better separation resolution, portability, and disposability^{3,8}. Also, they hold promise of integrating several chemical and biological analysis steps into a micro total analysis system (μ TAS, also called 'Lab-On-a-Chip') on one single chip.

Rationale for moving down the scale from microfluidics to nanofluidics is clear because it is important to approach a molecular level (1~10 nm) in order to understand many fundamental biological processes, for example, translation, gene regulation, mitosis, and cell communication³. Availability of nanofluidic tools with a similar size dimension as the target biomolecules and organelles, will allow better manipulation of these systems in general. In addition, nanofluidic tools might be significant due to the promise of the discovery of new phenomenon, which has not ever been seen at micro or macro scales. It is clear that there is a great deal of information about the mechanisms of the biomolecular activities that can only be uncovered by studying single molecules, which is conceivable with the development of nanofluidic tools. Understanding molecular transport will reveal new thrusts of applied research, such as single molecule

sequencing and molecular separation. Thus there is ample motivation to explore molecular transport in nanoscale structures.

It is feasible to create regular nanostructures on the scale between 10 nm and 1000 nm, by using the micro/nanofabrication techniques from the silicon industry and other nonconventional methods⁹⁻¹¹. The size of many biological particles, or organelles, such as lysosome (200 ~ 500 nm), secretory vesicles (50~200 nm), ribosome (~30 nm), virus particles (~50 nm), and DNA molecules, falls in this range⁸. In such a nanofluidic system, the interaction between fluidic structures and biomolecules becomes dominant over the interaction between the molecules and surrounding solvent, which dominates in a microfluidic system⁸. Therefore, it enables to manipulate and control biomolecules by incorporating carefully designed nanofluidic structures.

1.2 Fabrication of Nanofluidic Devices- Previous Works

Gels such as those made of agarose and cross-linked polyacrylamide (PA) were originally used as an anticonvective medium in slab gel electrophoresis. Currently, various types of gel with various pore sizes are widely used in biomolecular separation. However, it is generally hard to characterize or control the random pore structures of gels. Controlled polymerization enables the preparation of monolithic macroporous polymers with the desired chemistry and porous properties¹². These porous polymer monoliths have been developed as sieving media for various separation processes such as electrochromatography^{13, 14}.

Track-etched membranes offer distinct advantages over conventional porous membranes due to their precisely determined structures^{15, 16}. This track-etching process

consists of an irradiation of a polymer layer or a film by energetic heavy ions creating linear damage track, followed by a directional chemical etching of these tracks to pores¹⁶. The pore size, ranging from 10 nm to tens of micrometers, can be well controlled within ~15%⁸. Nanoporous nuclear-track-etched membranes are widely used to investigate molecular transport at nanometer scale structures^{17, 18}. Also, Au or carbon nanotubule membranes with a pore size down to molecular dimensions (~1 nm) were achieved via the template method based on track-etched membranes¹⁹⁻²⁴. However, the materials and the pore geometries of track-etched membranes are inherently limited¹⁵.

In contrast, micromachined nanofluidic structures offer unique advantages over random nanoporous material because of the possibility of advanced molecular control and the novel nanofluidic properties⁸. The nanofluidic structures can be precisely controlled. In addition, nanofluidics can be integrated with single molecule detection, which enables studying single molecules. A wide range of fabrication strategies with conventional lithographic methods and unconventional methods have been demonstrated so far. Han *et al.* generated a very thin channel with a depth of 75 nm for DNA entropic trapping by using standard photolithography²⁵. Turner *et al.* used monolithic sacrificial etching technique combined with e-beam lithography to generate ~50 nm fluidic obstructions²⁶. Austin *et al.* used focus ion beam (FIB) lithography to fabricate 50 nm nanoslits²⁷. Nanostructures also can be formed by electrochemical etching of silicon^{28, 29}. Alternatively, unconventional techniques have been developed. Cao *et al.* used nanoimprint lithography and nonuniform deposition technique to generate sealed nanochannels as small as 10 nm by 50 nm³⁰. Park *et al.* defined periodic arrays of holes with a small diameter of 20 nm by block copolymer lithography³¹. Jeon *et al.* fabricated

complex three-dimensional nanostructures with feature sizes as small as 50 nm by using high-resolution conformable phase masks³². Nykypanchuk *et al.* produced spherical cavities interconnected by circular holes to study DNA brownian motion by colloid templating³³. Saleh *et al.* embedded a nanoscale pore in PDMS with micromolding techniques³⁴.

1.3 Application of Nanofluidics

Nanoscale pores or nanofluidic channels have been used to detect single molecules as a molecular sensor. Martin group (University of Florida) fabricated nanotubules with internal diameter of a few nanometers, using an electroless gold plating method, to separate small molecules on the basis of both the molecular size and charge¹⁹⁻²⁴. Ion permselectivity was realized in a nanotubule membrane with a pore size of molecular dimension less than 1 nm, thus enabling to manipulate molecular transport. Also, Kasinanowicz *et al.* used a 2.6-nm diameter ion channel protein embedded in a lipid membrane to enable direct, high-speed detection of the sequence bases in single molecules of DNA or RNA³⁵. While this is achieved with natural pore proteins, effort is under way by the same group to implement this technique in artificially fabricated nanopores. Saleh *et al.* demonstrated a nanofluidic particle coulter counter to qualitatively sense individual nanoscale colloids³⁶. They also developed a nanoscale pore of 200-nm diameter in PDMS to sense electronically single DNA molecules³⁴.

In addition, nanofluidic devices have been successfully applied for biomolecular sieving and sorting. Han *et al.* developed a nanofluidic channel device with alternative narrow constrictions and wide regions to separate double-stranded DNA molecules by the

mechanism of entropic trapping^{25, 37-39}. Recently, Fu *et al.* used a nanofluidic filter array to achieve efficient separation of small DNA molecules and SDS-protein by steric hindrance mechanism⁴⁰. In addition to biomolecular separation, nanofluidic devices provide good platforms to study complex polymer dynamics. Hindered diffusion of molecules has been extensively investigated mostly using nuclear track-etched nanopores (one-dimensional nanospace)^{17, 33, 41-45}. Planar nanofluidic channels can provide uniform two-dimensional nanospace for careful study of molecular dynamics. Confinement on dynamics of polymers was studied by electrohydrodynamic stretching of single DNA molecules hooked in a thin nanochannel⁴⁶. Recently, Tegenfeldt *et al.* investigated the dynamics of genomic-length DNA molecules confined to a nanochannel with a diameter of 100 nm⁴⁷.

Nanofluidic devices can be coupled with various sensitive molecule detection (SMD) methods, such as two-photon fluorescence correlation spectroscopy (FCS) and near-field scanning optical microscopy, to allow better sensing and analysis due to the increased signal to noise ratio and higher sample concentration⁸. Lyon *et al.* reported restricted brownian motion of molecules in a sub-micrometer diameter capillary with confocal fluorescence microscopy⁴⁸. Foguet *et al.* demonstrated single molecule DNA fragment sizing in a submicrometer-sized fluidic channel by fluorescence correlation spectroscopy⁴⁹. Also, they demonstrated fast, high-throughput sensing and analysis of molecules passing a thin nanofluidic channel with FCS⁵⁰.

1.4 Thesis Objectives

The technique of fabricating planar, thin nanofluidic channels, described by Han *et al.*²⁵, is fairly standard, simple, and repeatable, and nanochannels made by this method are rather robust mechanically. The uniformity of the channels as well as the limit of this technique, however, has never been characterized. This fabrication strategy could potentially be applicable to other materials such as borosilicate glass. Additionally, one of the issues with this planar nanofluidic channel is its limited conductance and low throughput for biomolecular analysis.

The purpose of this thesis is to carefully test and characterize the applicability and limitation of PDMS micromolding and the substrate bonding techniques including both anodic (Si-glass) and thermal fusion (glass-glass) bonding, in fabricating sub-100-nm thick nanofluidic channels. The flat nanofluidic channels will be used to study dynamics of biomolecules confined in a nanoscale space. We also develop a novel fabrication strategy for generating massively-parallel nanofluidic filters with high fluidic conductance for high-throughput separation of biomolecules.

1.4 Thesis Outline

This thesis focuses on fabrication and characterization of sub-100-nm fluidic channels on PDMS, silicon and glass substrates, respectively. Chapter 2 describes the fabrication of nanochannels with PDMS material. We have characterized the minimum depth of nanochannels made from 184 PDMS and h-PDMS to withstand collapse. Next, Chapter 3 and 4 describe the fabrication of nanofluidic channels on silicon and glass substrates using anodic bonding and glass-glass bonding techniques. The uniformity of the channels

as well as the limit of these techniques has been characterized. In chapter 5, we have developed a fabrication technique that allows one to make a massively parallel, vertical nanofluidic channels, using anisotropic etching of (110) Si substrate. Separation results of DNA mixture in the nanofilter device have been presented. The last chapter covers concluding remarks, ongoing work, and suggestions for future work to improve the performance of the device as well as potential applications.

Chapter 2 Fabrication of PDMS Nanofluidic

Channels

Poly(dimethylsiloxane) (PDMS) is one of the most widely used polymers for microfluidic applications. In this chapter, applicability of PDMS micromolding technique has been investigated to fabricate very thin nanofluidic channels. The popular Sylgard 184 PDMS (Dow Corning) and hard PDMS (h-PDMS) developed by Schmid *at al.*⁵¹, with a higher modulus and greater surface hardness than 184 PDMS, were used and compared. We characterized the minimum depth of nanochannels made from 184 PDMS and h-PDMS to withstand collapse. It is found that the fabrication of nanofluidic channels using PDMS substrates is generally limited to the thickness of ~100 nm because of the softness of the materials. Also, the gas permeability of PDMS poses a significant challenge in the operation of the nanofluidic devices.

2.1 Background

Although materials such as silicon and glass are excellent choices for electronic and mechanical devices, non-traditional MEMS material such as polydimethylsiloxane (PDMS), polyurethane, polyimide, parylene, and polymethyl methacrylate (PMMA) are finding applications in various areas from microfluidics to nanofluidics because of their superior attributes and additional advantages^{11, 52-56}. In particular, PDMS has been one of the most actively developed polymers for microfluidic applications⁵³. PDMS devices are

fabricated by replica molding, a technique that allows inexpensive and rapid phototyping of microfluidic devices^{54, 56}.

PDMS materials have many distinctive attributes that make them ideally suited for micro/nanofluidic systems. Firstly, PDMS is inexpensive, 50 times cheaper than silicon on a per volume basis. The techniques of fabrication in PDMS material are easy and quick, and features can be reproduced with sub-100-nm fidelity in PDMS by replica molding⁵⁶, which makes mass-produced devices inexpensive. Secondly, the elastic property of PDMS is useful for certain microfluidic applications such as mechanical valve and pump⁵⁷. PDMS makes conformal contact with smooth plastic or glass substrates reversibly, while irreversible, permanent sealing by plasma oxidation is also possible. Thirdly, PDMS is compatible with most optical detection methods, including fluorescence correlation spectroscopy, since it is transparent in the visible and UV region. Finally, PDMS is bio-compatible because PDMS is nontoxic to cells and is gas-permeable. In addition, PDMS surface chemistry can be controlled by reasonably well-developed techniques, which enables us to change the surface charges easily.

However, the softness of PDMS can be problematic for the fabrication of nanofluidic systems with submicrometer sized features. The low elastic modulus of PDMS causes shallow relief features of a stamp to deform, buckle, or collapse⁵⁸. Sylgard 184 PDMS proved to be too soft to define features smaller than 500 nm^{58, 59}. Schmid *et al.* formulated alternative PDMS (h-PDMS) with a Young's modulus of 9.7 MPa for high-resolution soft lithography⁵¹. Based on this hard PDMS, Schmid generated square posts with a critical dimension as small as 80 nm, but a rather low aspect ratio of 1.25 was required for success^{51, 59}. Also, Odom demonstrated composite stamps composed of a h-

PDMS stiff layer supported by a 184 PDMS flexible layer to generate free-standing features down to 50 nm by phase-shifting lithography⁵⁸. However, the applicability of PDMS for fabricating regular nanofluidic channels down to 100 nm has never been completely investigated.

2.2 Fabrication Process

2.2.1 Overview of Fabrication Process

The fabrication process is summarized as follows: (1) Design and draw the photo masks with L-Edit Pro Version 10 (Tanner EDA, CA); (2) Transfer the mask layout onto a high-quality chrome mask (1 μm minimum feature, Microtronics Inc, PA); (3) Fabricate the silicon masters for PDMS micromolding in the cleanroom (Microsystems Technology Laboratories, MIT); (4) Treat the master surface with HMDS (hexamethyldisilazane) and perform PDMS molding over the master; (5) Make holes and seal PDMS against glass substrate. The detailed process and preparation of PDMS are listed in the Appendix.

2.2.2 Fabrication of Silicon Masters

The photo masks were designed and drawn by using the software L-Edit Pro Version 10 (Tanner EDA Inc., CA) and then transferred onto a chrome mask. The photomasks were written at the 0.25 μm spot size (Microtronics Inc, PA) so that the features with the 1 μm resolution can be achieved. The image reversal photoresist AZ5214E was coated on 6" silicon wafers and exposed by UV contact lithography (EV620 with an intensity of 10

mWcm⁻²sec⁻¹ and a wavelength of 365-405 nm). Masters for nanochannels with various depths were made on silicon wafers by using reactive ion etching (RIE) technique (LAM 490B). The thickness of the channels can be changed and optimized by controlling the etch parameters. It is straightforward to fabricate the entropic traps with alternative thin and thick regions using the standard photolithography and RIE techniques developed by Han *et al.*²⁵. A brief outline of the process steps is shown in Fig 2.1.

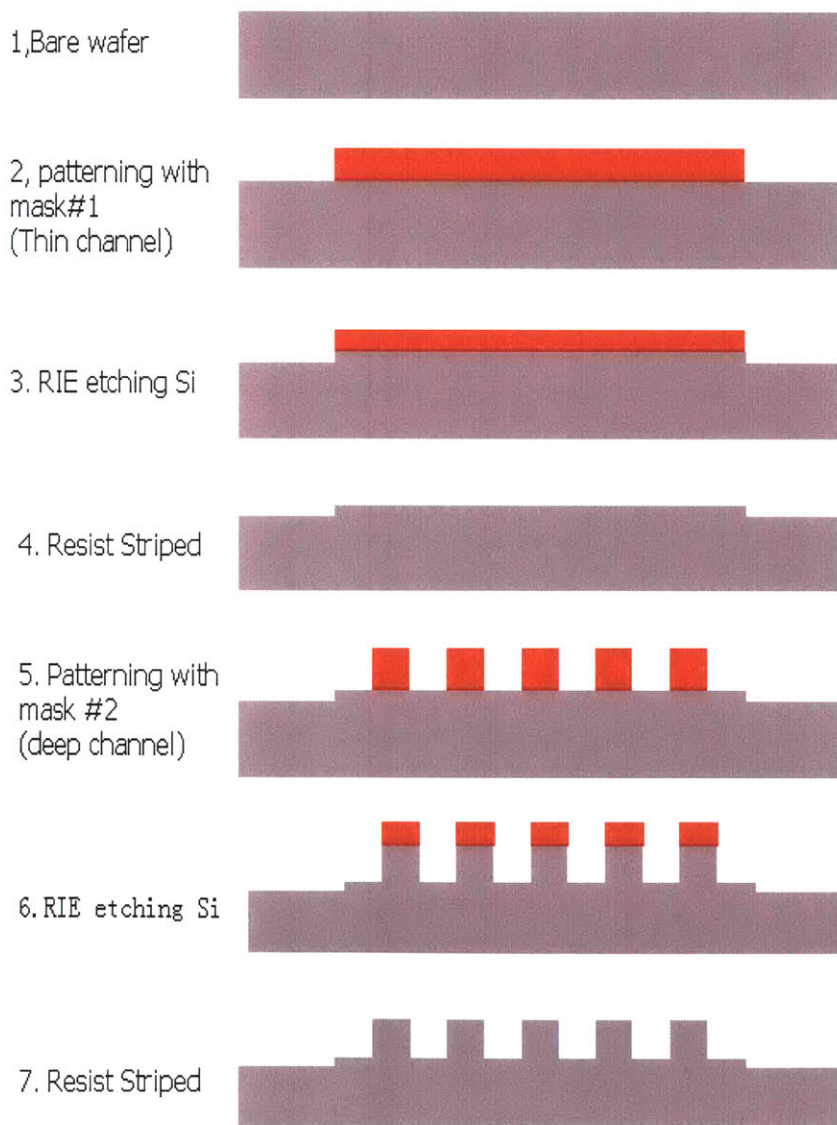


Figure 2.1 Fabrication process of silicon masters for PDMS micromolding

2.3 Results and Discussion

PDMS nanochannels with various widths and depths were fabricated to explore the minimum depth for Sylgard 184 and h-PDMS to withstand collapse. Table 2.1 summarizes the results of the generated features with both Sylgard 184 and h-PDMS. An important parameter here is the ratio between the channel depth and width, which is the aspect ratio of the nanochannel. If the channel has supporting pillars to prevent collapsing, inter-pillar distances were used to calculate the aspect ratio. It is shown that flat nanochannels with the depth of less than 500 nm, made of flexible Sylgard 184 with a Young's modulus of 3 MPa, tend to collapse, which is in good agreement with the results from Xia *et al.*⁵⁶ and Michel *et al.*⁵⁹. While using the h-PDMS with a Young's modulus of 9.7 MPa, we could generate simple nanochannels with critical dimensions down to 110 nm and aspect ratio of 25 as shown in Figure 2.2 (a) and (b). It has been reported that two-layer composite PDMS stamps from h-PDMS and 184 PDMS patterned with 1 μm lines spaced by 1 μm were able to withstand collapse down to 120 nm⁵⁸ and h-PDMS allowed the definition of useful reliefs down to 80 nm with an aspect ratio of 1.25⁵¹. Our results are quite consistent with their achievement. The aspect ratios of relief structures on PDMS substrates were found to be between about 0.2 and 2 for defect-free stamps⁵⁶. However, a larger aspect ratio was achieved here.

Table 2.1 Comparison of Sylgard 184 PDMS and h-PDMS

Nanofluidic channels	Aspect Ratio ^c	Sylgard 184 PDMS	h-PDMS	
			Before filling	After filling
30 μm wide, depth larger than 600 nm ^a	~ 50	Survive	Survive	Survive
30 μm wide, 500 nm deep ^a	~ 60	Collapse	Survive	Survive
30 μm wide, 350 nm deep ^a	~ 85	Collapse	Survive	Collapse
3 μm wide, 350 nm deep ^a	~ 8.5	Collapse	Survive	Survive
3 μm wide, 225 nm deep ^a	~ 13	Collapse	Survive	Collapse
3 μm wide, 225 nm deep ^b	~ 13	Collapse	Survive	Survive
3 μm wide, 110 nm deep ^b	~ 27	Collapse	Survive	Collapse
3 μm wide, 100 nm deep ^b	~ 30	Collapse	Collapse	Collapse

^a Flat channels; ^b Alternative thin and thick channels. The given depth is the thickness of thin channels. The depth of thick channels is 1.4 μm . ^c The aspect ratio is defined as the ratio of the width to depth of the pattern.

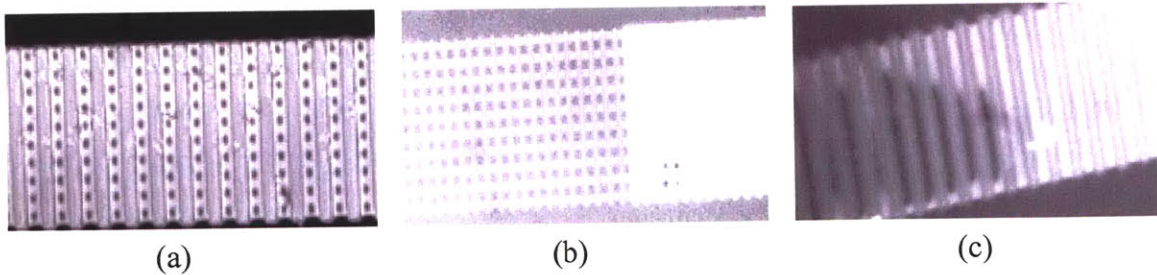


Figure 2.2 Optical micrograph of h-PDMS nanofluidic channels with alternative thin and thick regions (1.4 μm in thick region and 110 nm in thin region) (top view). **a)** The width of the channel is 50 μm and the period of the channel is 8 μm . Supporting pillars with 1 $\mu\text{m} \times 2 \mu\text{m}$ in the thin region are spaced by 3 μm . **b)** The width of the channel is 30 μm and the period of the channel is 6 μm . Thin regions consist of 3 μm lines spaced by 3 μm . The left part was filled with DI water while the right part was not filled yet. **c)** The bright channel was filled and survived, while the dark channel collapsed. No pillars.

The extension of the PDMS fabrication technique to generate nanofluidic channels in the sub-100nm thickness range is greatly limited by its low Young's modulus even for h-PDMS. Three typical deformations due to the low modulus of PDMS materials, including roof collapse, lateral collapse, and rounding by surface tension, were described by Odom *et al*⁵⁸. However, even when the nanofluidic channel survived the bonding process, it is prone to collapse during the filling process of the channel, which can be clearly seen from Table 2.1 and Figure 2.2(c). We believe that this is due to surface tension of liquid-gas interface during the filling process. Since PDMS surface and glass substrate become rather hydrophilic after oxygen plasma treatment, water is introduced into the nanochannel by the strong tensile surface tension. As shown in Figure 2.3 (A), the negative pressure of water plug was generated in the nanochannel, as a result, and caused bending of the PDMS layer surrounding the channel, which results from the curvature of the liquid meniscus⁶⁰. As the water-air interface proceeds, the strong surface tension can pull down the roof and induce systematic collapsing in front of the water-air filling boundary. Once a small, bonded region between the top and bottom of the nanochannel formed, that region quickly propagated to the entire nanochannel, inducing complete collapse. We also tested the fabrication of nanofluidic channels with alternate thin and thick regions, as used in previous DNA experiments²⁵. They have better yield in bonding process, which can be shown from higher aspect ratio and smaller thickness possible in Table 2.1, since the propagation of collapsed region is somewhat prevented by the existence of thick regions. However, even though it was possible to fabricate ~100 nm thick nanofluidic channels using the proper aspect ratio and h-PDMS material, the

experiment in such a device was severely limited by this collapse during the channel filling process.

Another serious practical issue with PDMS nanochannels is the high porosity of PDMS material. While advantageous in some applications (cell culture microdevices, for example), the gas permeability of PDMS means that liquid within the channel can evaporate and permeate away through the substrate. We found that substantial and non-negligible fluid flow moving from two reservoirs to the center was generated and accumulated in the center without any external applied force, as shown in Figure 2.3 (B).

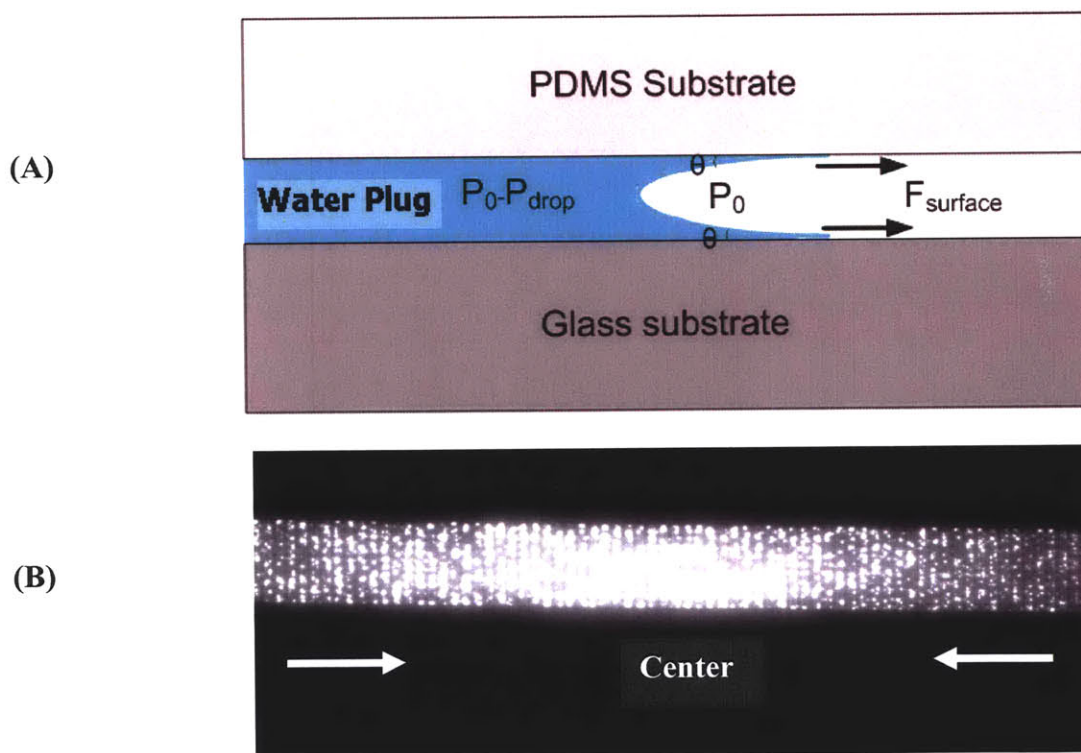


Figure 2.3 (A) Schematic description of water plug in a PDMS channel sealed with glass substrate (side view). Θ is the contact angle. The surface tension F_{surface} results in the meniscus curvature and a pressure drop. (B) Fluorescence image of phycoerythrin protein in a PDMS channel. Due to the evaporation, protein moved towards the center from both reservoirs without any applied electrical field and accumulated in the center region.

It was demonstrated to be due to the evaporation effect^{61, 62}. Also, it was reported that osmosis and pervaporation of water through the roof of polyimide submicron channels caused a liquid flow with a 2~4 $\mu\text{m}/\text{sec}$ flow rate and a concentration change⁶³. This effect is usually negligible and not typically noticed in the microfluidic channel made from PDMS, but becomes significant in thin nanofluidic channels due to the larger surface-to-volume ratio of such channels. Moreover, the flow rate is not uniform across the whole channel length and decreases as fluid moves toward the middle of two reservoirs. The average velocity in a flat PDMS channel as a function of the channel depth and the position along the channel direction was derived and examined by Randall *et al*⁶¹. This translational flow also caused sample absorption, and rendered any (FCS, for example) experiment very difficult to reproduce. Although soaking PDMS at 65 °C hot water can prevent fluid flow due to evaporation somehow⁶², it will be effective only for a couple of hours.

2.4 Conclusions

Detailed fabrication technique of making nanofluidic channels with PDMS material was described in this chapter. We compared nanofluidic channels made by both Sylgard 184 and h-PDMS using replica molding technique. We found that it is difficult (even for h-PDMS) to generate free-standing nanochannels down to 100 nm, although h-PDMS has three times higher modulus than Sylgard 184. In addition, strong surface tension tends to pull down the roof and induce systematic collapsing during the nanochannel filling process. We also showed that the translational flow and sample absorption caused by the liquid evaporation through PDMS substrate critically prevented the molecular sieving and

other (FCS) experiments in the PDMS nanochannels. Therefore, it was concluded that the PDMS substrate is not well-suited for the application of nanofluidic molecular sieving and scientific studies of molecular transport in confined spaces.

Chapter 3 Fabrication of Nanofluidic Channels on Silicon Substrate

Since the fabrication of nanofluidic channels using PDMS substrates is generally limited to the thickness on the order of 100 nm, silicon is used to fabricate nanofluidic channels with the depth down to 100 nm. A technique of fabricating very thin channels using silicon-based standard photolithography, reactive ion etching, and anodic bonding techniques has been explored by Han *et al.*³⁷, and successfully applied to the separation of large DNA molecules^{25, 38, 39}. While the fabrication of nanofluidic channel as thin as 30 nm has been achieved by Han⁶⁴, the uniformity of the channel as well as the limit of this technique has never been characterized. Considering the strong field (and strong force involved in the bonding process) used in the bonding process, the channel might sag and as a result, the depth of the channel might change.

This chapter describes the fabrication technique of making thin nanofluidic channels on silicon substrate. We investigated the ultimate minimum thickness one could achieve using this fabrication technique. Scanning electron micrograph imaging was used to measure the depth of nanochannels after anodic bonding process in order to investigate whether the bonding process (at high field and temperature) would change the depth of the nanochannels defined in the Si substrate. It was shown that this fabrication strategy can be used reliably to make nanofluidic channels as thin as 20 nm. The aspect ratio of the nanochannel was limited to be ~250 in this case. While the fabrication technique by anodic bonding is robust and repeatable, nanofluidic channels made by this technique

have several limitations caused by semiconducting, non-transparent Si substrate. For example, unexpected strong background signal from silicon substrate at the infrared wavelength (700~900 nm) for two-photon fluorescence correlation spectroscopy (FCS) was observed, which prevented us from performing FCS within nanochannels on silicon substrate.

3.1 Anodic bonding: Applications and Mechanism

Anodic bonding is a well-known substrate bonding method between Si and glass wafers. It was first reported almost 35 years ago⁶⁵, and this method has been extensively applied to various MEMS and other packaging applications for microelectronics and microfluidics systems^{1, 66-68}. Compared to direct bonding, anodic bonding has the advantage of being a lower temperature process with a lower residual stress and with less stringent requirements for the surface quality of the wafers⁶⁹.

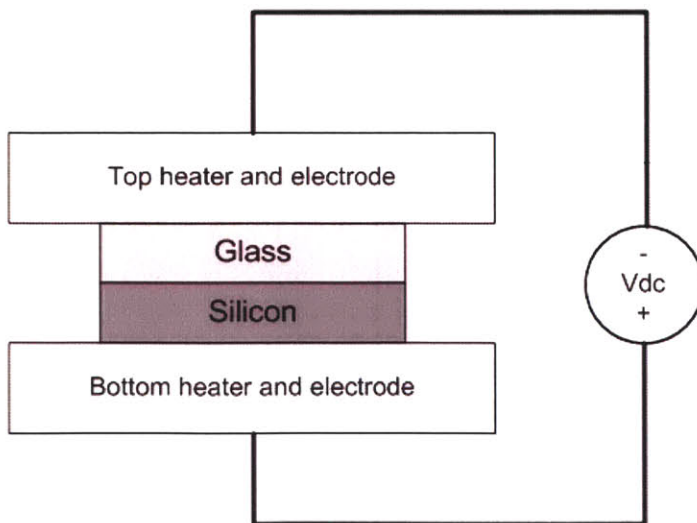


Figure 3.1 Schematic diagram of anodic glass-silicon bonding. Control parameters are temperature, materials and bias voltage.

Typically, anodic bonding requires high temperature (300~400 °C) and high electric field (400-1000 V) to generate a permanent bonding between silicon wafer and glass. Figure 3.1 represents a schematic of anodic bonding setup. Generally, the stacked silicon and glass substrates are assembled and heated on a hot plate to a certain high temperature (~350 °C). A DC power supply is connected to the assembly such that the silicon is positive with respect to the glass wafer. When a voltage on the order of a few hundred volts is applied across the assembly the glass seals to the silicon substrate permanently.

The mechanism involved in the bonding process is attributed to mobile ions in the glass^{69, 70}. It is suggested that at elevated temperature the glass becomes a conductive solid electrolyte. The mobile positive alkali ions in glass wafers migrate toward the cathode due to the applied voltage and leave a space charge (bound negative charges) in the region of glass-silicon interface. As a result, most of the applied voltage drop occurs across this space charge region and the high electrical field between the glass and silicon causes a strong electrostatic force to pull the glass and Si into intimate contact. As a result, covalent, permanent bonding is formed between the two substrates.

The bonding method will work only with certain type of glass materials, because of the required thermal matching between Si and glass. Typically borosilicate glass materials (for example, Corning 7740 Pyrex) are well suited for anodic bonding. Various aspects of anodic bonding process have been studied extensively. Rogers *et al.*⁷¹ examined the optimal glass materials for obtaining good bonds. Anthony *et al.*⁷² discussed quantitatively the effects of the electrostatic forces and surface imperfections. Anodic bonding process between glass and thin-film coated silicon substrates was characterized in detail by Lee *et al.*⁷³. Also, Wei *et al.*⁷⁴ discussed the role of bonding temperature and

voltage in anodic bonding. Li *et al.*⁷⁰ presented a theoretical model to study the effects of bonding parameters, including bonding temperature, applied voltage, and bonding time, on the electrostatic force. Recently, Shih *et al.*⁷⁵ established a criterion for the microchannel collapse, in terms of applied voltage and the width and depth of the channel as well as material constant, by carrying out a detailed electromechanical analysis and experimental observations. The criterion can be applied to microscale fluidic channels, however, and it is not clear whether it still holds for nanofluidic channels. Furthermore, the limit of the anodic bonding technique for fabricating nanochannels has yet been investigated.

3.2 Fabrication Process

For the feasibility test of the anodic bonding for the fabrication of nanofluidic channels, patterns with various aspect ratios (width to depth) has been transferred and etched into shallow trenches on Si substrate. A schematic diagram of the fabrication process is given in Figure 3.2. First, silicon wafers were cleaned in a piranha solution (H_2SO_4 (%): H_2O_2 (%) =3:1) for 10 min, rinsed in DI water and spun dry with nitrogen gas. Then nanofluidic channels with various widths and depths were patterned and etched into silicon wafers by using standard photolithography and reactive ion etching (RIE) techniques. It is straightforward to control the depth of the channel, since the etch parameters can be controlled easily. After patterning of the channels, potassium hydroxide (KOH) etching technique was used to make access holes from the backside of the wafer. Then a thermal oxide layer was grown to provide an electrical isolation between silicon substrate and biomolecular solution. Finally, after piranha cleaning for 10

min, the silicon device was bonded to a flat glass plate (Pyrex Corning 7740 or Borofloat, Sensor Prep Services, Inc., IL) by anodic bonding technique. The bonding process was carried out at 350 °C with an applied voltage of 800 V in the bonder machine (EV501, Electronic Vision group). Depth measurement of the fabricated channels was performed before anodic bonding with the surface profilometer (Prometrix P-10, KLA-Tenco Co., CA.). All the fabrication process except bonding was done in the cleanroom of MTL. The detailed process flow is described in the Appendix.

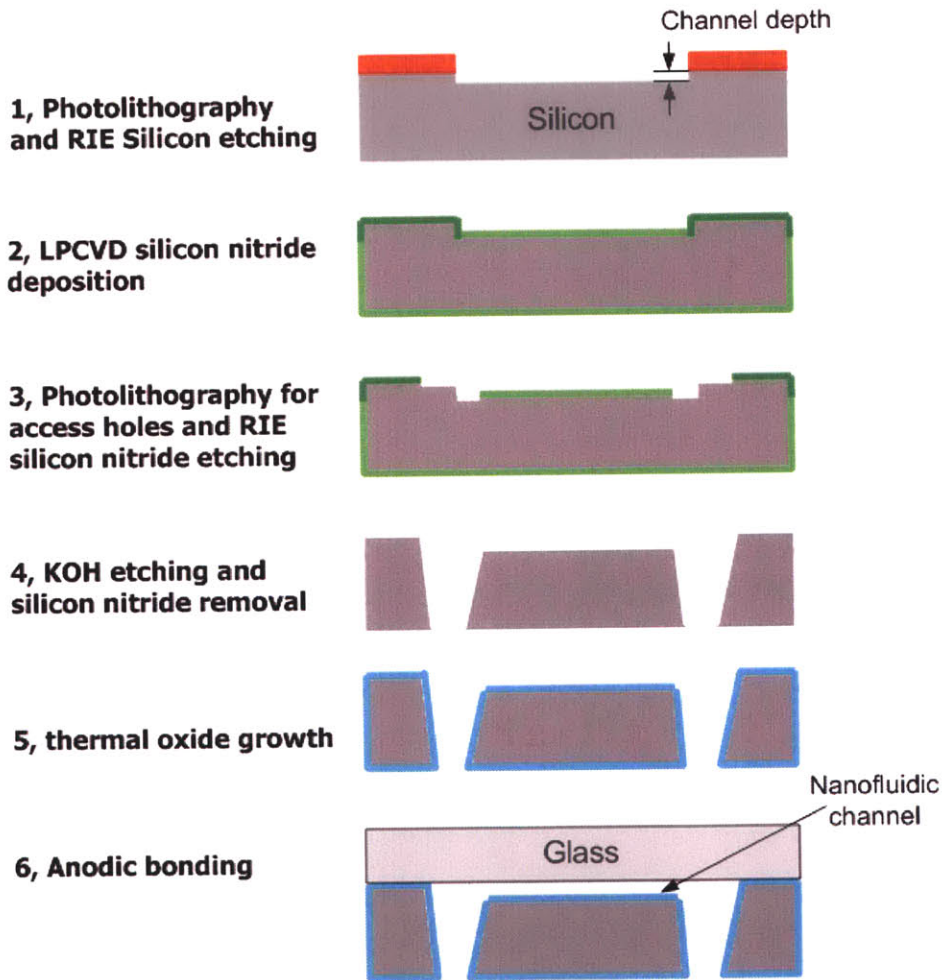


Figure 3.2 Fabrication process of nanofluidic channels on silicon substrate

3.3 Results and discussion

3.3.1 Characterization of Nanochannel Fabrication

We fabricated nanochannels with various widths and depths to investigate the limit of this fabrication technique in the normal bonding condition. Table 3.1 summarizes the results of the survival or collapse of the channels with various depths and widths by optical inspection. The optical micrograph of the typical success or failure of nanochannels is shown in Figure 3.3. The channels turned from bright to gray when they collapsed. Once its roof makes contact, a channel collapses quickly and completely due to the attractive interfacial surface forces, except the narrow region along the edge⁷⁵.

Table 3.1 Survival or collapse of the nanofluidic channels ^a after anodic bonding ^b

Channel depth	Channel width						Maximum aspect ratio
	3 μm	5 μm	10 μm	20 μm	50 μm	200 μm	
180 nm	Survive	Survive	Survive	Survive	Survive	Collapse	278
80 nm	Survive	Survive	Survive	Survive	Collapse	Collapse	250
40 nm	Survive	Survive	Survive	Collapse	Collapse	Collapse	250
20 nm	Survive	Survive	Collapse	Collapse	Collapse	Collapse	250

^a The channels consist of 2 cm long parallel lines spaced by 5 μm .

^b Bonding Condition: 6" Borofloat glass; 390 nm oxide grown on <100> silicon wafers; 350 °C, 800 V; 2000 N pressure force; EV501 Bonder machine.

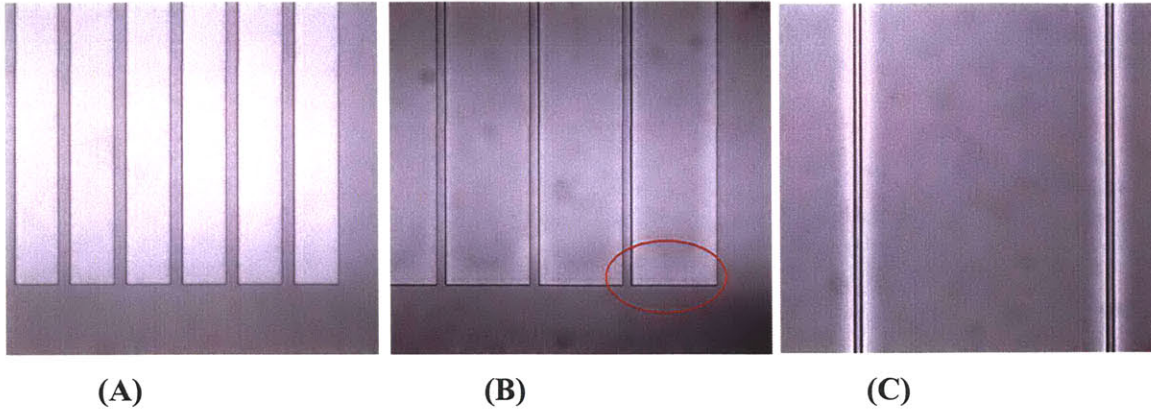


Figure 3.3 Optical observation of the survival or collapse of the channels. (A) Survived channels with the depth of 80 nm and width of 20 μm , spaced by 5 μm . (B) Collapsed channels with the depth of 80 nm and width of 50 μm , spaced by 5 μm . Very small areas along the edge did not collapse. (C) The entire channels, 200 μm in width and 180 nm in depth, collapsed except along the edge. The channels turned from bright to gray when they collapsed.

Nanofluidic channels as thin as 20 nm with rather high aspect ratio (more than 250:1, width to depth) have been achieved with this technique, which is smaller than 30 nm nanofluidic channels reported by Han⁶⁴. This result is significant since the aspect ratio of the nanochannel is much larger than the previous reports where several researchers reported fabrication of nanochannels with low aspect ratio (similar width and depth)^{30, 76}. It is also shown that the aspect ratio of the channel (width/depth) is an important factor to determine the success or failure of the fabrication. The maximum aspect ratio of surviving channels with varying depths is around 250, which is rather consistent for different depths from 180 nm down to 20 nm. Our results do not conform to the criterion for the collapse developed by Shih *et al.*⁷⁵, showing the collapse can be avoid as long as

the ratio of the width of channel to the cube of the depth of the channel is less than some constant associated with the applied voltage and material constant. A more detailed model might be needed to establish the criterion for the collapse of nanochannels. It is not clear whether 20 nm is the ultimate minimum thickness that can be attained from this technique. Further investigation is under way to test the possibility of fabricating nanochannels as thin as 10 nm or even thinner channel thickness.

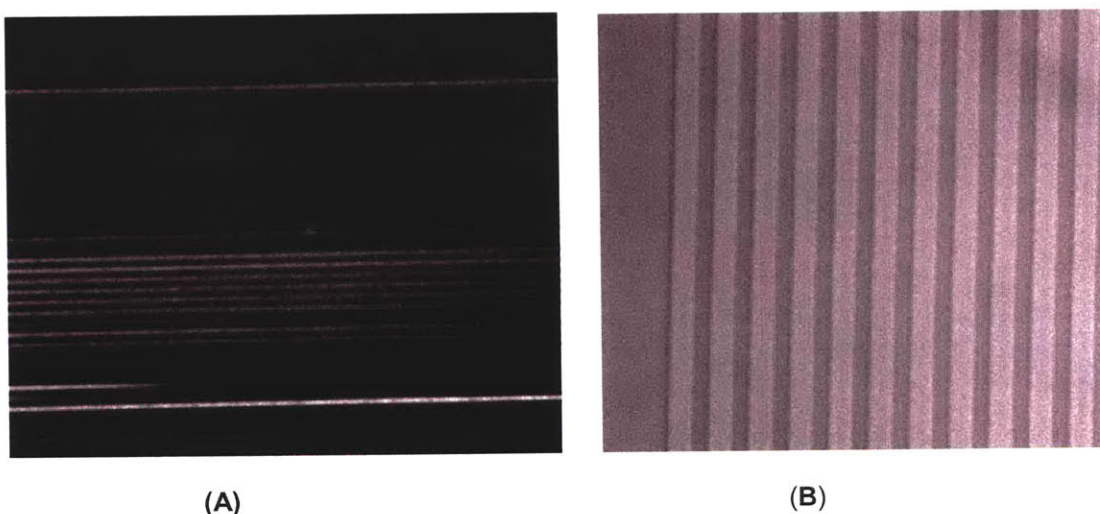


Figure 3.4 (A) Fluorescence imaging of 20 nm deep nanofluidic channels being filled with concentrated FITC dye in TBE 5X buffer solution. Due to a strong capillary force, buffer solution as well as dye molecules spontaneously filled the entire nanofluidic channel without any external driving force. The width of individual channels is 3 μm spaced by 3 μm . (B) (Bright field) microscopic image of 20 nm deep silicon nanofluidic channels spaced by 3 μm . The width of individual channels is 5 μm .

In addition, we succeeded in filling channels to make sure the nanochannels survived. Figure 3.4(A) shows the fabricated 20 nm nanofluidic channels and the filling of the channel with concentrated FITC dye in TBE 5X buffer solution. Due to the strong

capillary force, buffer solution as well as dye molecules were introduced to the 20-nm-deep nanofluidic channel without any external driving force. It was possible to fill the entire length of 1-2 cm long, 3 μm wide and 20 nm deep nanochannels within 20 minutes.

It is interesting to see that when the channel fabrication failed due to the sagging (caused by too large aspect ratio) the entire channel region gets sagged down. While the temperature for anodic bonding is much lower than the glass transition temperature ($\sim 550\text{C}$), applied electric field exerts a strong force between the walls of the nanochannel during the bonding process. If the aspect ratio is larger than a certain critical number, bending of the top surface could cause the contact between top and bottom surface, which will instantly be bonded permanently at this condition. Once a small contact occurs, the contact area could be quickly expanded across the entire device, and could lead to a complete bonding between the top and bottom walls of the nanochannel. In that sense, decreasing the bonding potential might lead to somewhat better success rate for large aspect ratio channels, but this is yet to be tested. Bonding temperature and pressure would be other important factors in affecting the success of the structure, as demonstrated by previous research^{70, 75}. We have not tested two effects yet. However, as one of our future plans, more efforts are to be taken to identify the capability and practical limitation of fabricating nanofluidic channels using anodic bonding methods.

3.3.2 Depth Measurement after Anodic Bonding

The depth of nanochannels shown above was measured by using P10 Tencor surface profilometer (with high vertical resolution less than 5 \AA) before the anodic bonding step. However, the actual thickness after bonding could be smaller than, or the same as the

thickness measured before bonding, due to the potential reflow of glass materials caused by relatively high bonding temperature (~350 °C). An exact measurement technique for the nanofluidic channels would be desirable for better experimental analysis. Scanning electron microscopy (SEM) imaging was used to measure and confirm the thickness of nanofluidic channels after the bonding process.

A new photo mask, full of parallel lines spaced at several microns from each other, as shown in Figure 3.5, was designed to make it easy to locate channels while SEM imaging. Hence, no matter where we look, we always have a channel in view when we inspect the bonding surface. Devices with this new design were made by exactly following the same fabrication process as above. After bonding the silicon wafer with a glass cover, wafers were cut to reveal the cross section of the bonded nanochannels, using diamond glass cutter and diamond wafer scribe. A clean, smooth cross section could be revealed with this cutting method. In order to achieve better imaging from insulating glass materials, the devices were coated with a thin layer of gold occasionally. However, the SEM imaging contrast between glass and silicon substrates disappeared after the gold coating, and it becomes hard to locate Si-glass bonding boundaries where the nanochannels are located. A way to find the channels is to cover a part of the nanochannels with aluminum foil while coating gold. Then, the glass-silicon boundary in the foil-covered region is visible (due to the conductivity difference between Si and glass) so that nanochannels can be easily located. Afterwards, nicer SEM imaging can be done in the gold-coated surface.

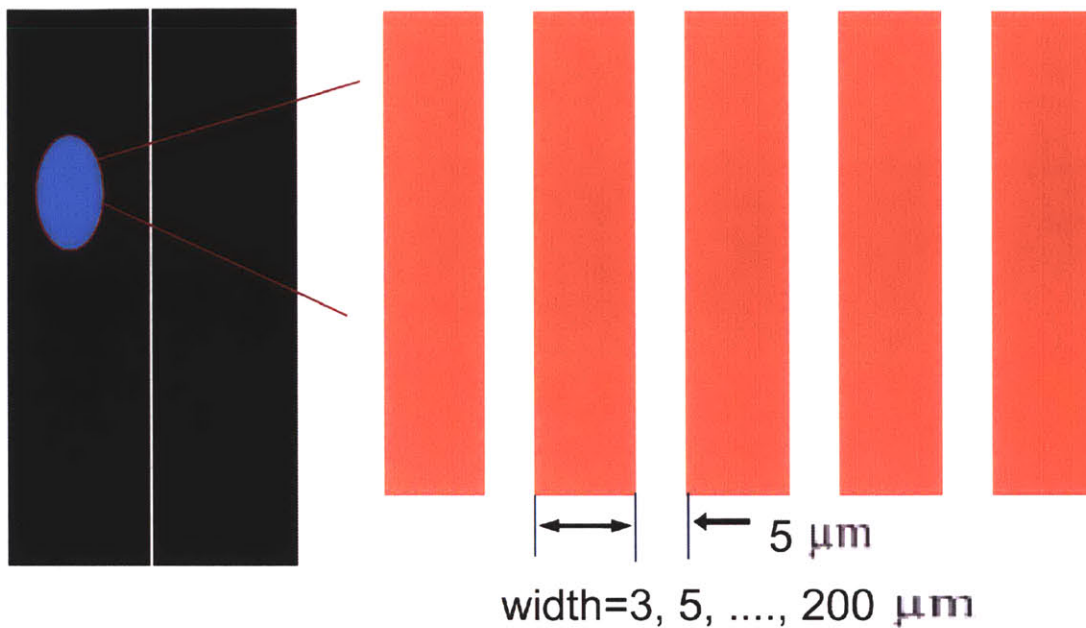


Figure 3.5 Layout of the test pattern consisting of an array of 2 cm long parallel lines with various widths spaced at 5 μm from each other.

Nanochannels with various depths from 180 nm down to 20 nm have been made to investigate the possible change of the depth due to anodic bonding process. The cross-sectional SEM images of nanochannels with various depths are shown in Figure 3.5. It can be seen that the channels are of good uniformity and completely open and there is no significant deformation or sagging of the wafers, even for 20 nm deep channels. According to Table 3.2, the comparison of the depths of nanochannels measured before bonding and after bonding shows that no significant change of the depth due to the bonding process can be observed, considering 10 % variation acceptable, which is caused by noise both in SEM images and profilometer measurement. Hence, it is proved that anodic bonding process in our bonding condition causes little effect on changing the depth of the nanochannel if a proper aspect ratio of the channel is maintained.

Table 3.2 Comparison of nanochannel depths before bonding and after bonding

Nanofluidic channels	Measured depth before bonding (P10)	Measured depth after bonding (SEM)
"180 nm"	180±5 nm	173±5 nm
"80 nm"	82±2 nm	75±5 nm
"40 nm"	44±2 nm	40±4 nm
"20 nm"	20±2 nm	20±4 nm

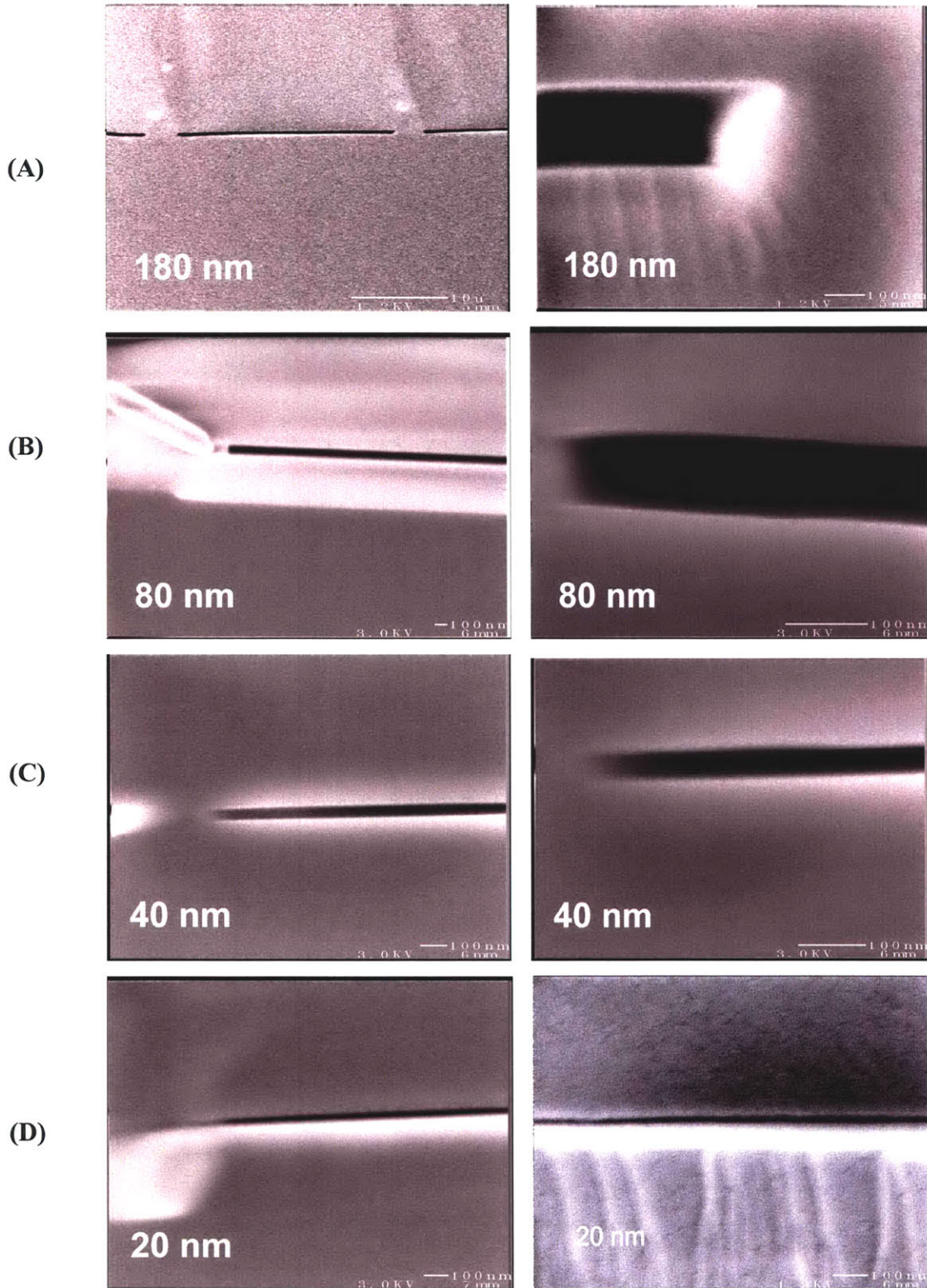


Figure 3.6 Cross-sectional SEM images and close-up of nanochannels with the depth of 180 nm (A), 80 nm (B), 40 nm (C), and 20 nm (D) on silicon substrate (bottom wafer) bonded to a borofloat wafer (top wafer), respectively.

3.3.3 Limitation of Silicon-Glass Nanofluidic Channels

The anodic bonding technique provides a reliable way to fabricate nanofluidic channels as thin as 20 nm reliably. However, the use of silicon-glass nanochannels is limited for certain applications.

1) Si is a semi-conducting material such that it requires a thin insulation layer such as oxide or silicon nitride to provide an electrical isolation between silicon substrate and fluid solution in micro/nanofluidic systems, especially in the case of electrophoresis devices. However, these intermediate layers between silicon and glass substrates will have significant effects on the quality of anodic bonding^{73,77}. In order to achieve effective bonding, the oxide thickness should be limited below 1 μm . Even with this maximum oxide thickness, one cannot apply thousands of volts to the device without shorting out the devices. Therefore, silicon-glass channels cannot be used in the applications, which require very high electrical voltage applied. The thermal fusion bonding of glass and silicon substrate can overcome this limitation of the thin oxide layer.

2) Si is not a transparent substrate, which sometimes causes background for non-visible optical measurement. For example, in the two-photon fluorescence correlation spectroscopy of the molecules within the nanofluidic channels fabricated on silicon substrate, it was discovered that the silicon substrate exhibited very high levels of background signal, especially in the wavelength region of 800~900 nm, which is the excitation wavelength for two-photon FCS. The bandgap for silicon is about 1200 nm,

but there are also gaps at around 600 nm and 355 nm, which could potentially pose a problem with two photons.

3) The glass materials are limited to borosilicate glass (Pyrex or Borofloat). These borosilicate glass materials are a multicomponent mixture of SiO_2 and other metal oxide (Na_2O , CaO , MgO , and Fe_2O_3), which is typically not CMOS-compatible. Moreover, Pyrex has very poor transmission in the UV range (wavelength less than 330 nm), so the optical detection method is limited.

Chapter 4 Fabrication of Nanofluidic Channels on Glass Substrates

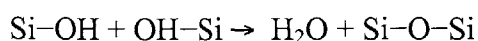
In many applications, micro/nanofluidic devices made out of all glass substrates are preferred over silicon due to its mechanical strength, optical transparency, and non-conductivity. In this chapter, we characterized a well-known glass-glass fusion bonding process at high temperature for the fabrication of sub-100-nm fluidic channels on glass substrate. Effective bonding between two glass substrates was achieved by annealing at 550 °C with a low ramp and cool-down rate. In addition, we investigated the minimum thickness of nanochannels that can be fabricated with this fusion bonding technique. SEM measurement has been conducted to characterize the uniformity and the thickness of the etched channel after bonding, and it was proved that the technique can be used to fabricate nanochannels as thin as 25 nm, with aspect ratio as large as 2000. Also, there was no significant change of the depth of the channel observed, before and after the fusion bonding process.

4.1 Glass-Glass Bonding

Direct bonding, also termed as wafer bonding or fusion bonding, refers to the phenomenon wherein mirror-polished and clean wafers of almost any material, when brought into contact at room temperature, are attracted to each other by van der Waals forces and adhere or bond to each other⁷⁸. This phenomenon has been well known for a long time for optically polished materials and was first investigated for quartz glass by Rayleigh in 1936⁷⁹. Direct bonding method has been widely used since it opens a wide range of new possibilities for fabrication and integration of semiconductor devices and MEMS devices^{80, 81}. Compared to anodic bonding, it also provides high bonding strength but provide a more flexible choice of materials for bonding, even two dissimilar materials. The materials are not limited to semiconductors and can be present in single crystal, polycrystalline, or amorphous form. Wafer bonding may be performed via intermediate layers such as oxide, nitride, metals, and silicides⁸⁰. However, direct bonding requires more stringent cleanliness and flatness of the surfaces to be bonded.

Wafer direct bonding typically includes the follow steps. Firstly, the surfaces of two wafers are prepared with meticulous cleaning and brought into intimate contact at room temperature. Sometimes, moderate pressure can be applied to help achieve better adhesion. Finally, an appropriate annealing step is performed to increase the bonding strength. The anneal temperature might vary with the desired materials and applications.

At present the fusion bonding mechanism is not completely clear. However, the reaction of two surface silanol chemical groups is believed to be the main bonding reaction^{69, 78, 82}:



Silanol groups give rise to hydrogen bonding (hydrogen-bridge bonds), which takes place spontaneously even at room temperature. After dehydration, the silanol groups form siloxane covalent bonds. However, bonding at room temperature is weak and reversible. A further heating at elevated temperature results in much stronger siloxane bonds forming and also water molecules can be removed by diffusing through the oxide during heating^{69, 80}.

A number of glass-glass direct bonding techniques, including low temperature and high temperature bonding, have been extensively studied and developed. Wang *et al.* fabricated glass microchip devices with strong bonding and good channel sealing by employing sodium silicate as an adhesive layer at 90 °C⁸³. Huang *et al.* used a UV-curable glue to achieve glass microchip bonding at room temperature⁸⁴. Sayah *et al.* described two direct low temperature bonding techniques with epoxy gluing process and high pressure, respectively⁸⁵. Chiem *et al.* reported a room-temperature bonding procedure based on rigorous cleaning⁸⁶. Recently, Jia *et al.* achieved effective bonding of glass chips under a continuous flow of water at room temperature without the requirement of clean-room facility⁸². Usually, the low temperature bonding requires a rigorous cleaning procedure prior to bonding and the bonding strength could not be as large as high temperature bonding. Besides, the usage of adhesives or glue may clog the channels, especially for fabricating very thin channels. In contrast to low temperature bonding process, thermal fusion bonding at high temperature can provide good bonding strength and high bonding yield. Lin *et al.* succeeded in sealing microfluidic channels on soda-lime glass at 580 °C for 20 min with a slight pressure applied⁸⁷. Fan *et al.* achieved effective bonding between two Pyrex glass effectively at 640 °C after 6 hours⁸⁸.

Although glass-glass bonding at high temperature (around 600 °C for Pyrex) can be achieved successfully with large bonding strengths, the channels tend to be distorted and even collapsed since the glass material at this high temperature will be softened. Therefore, most of the above high temperature bonding techniques were mainly used for fabricating relatively thick microchannels (~10 μ m in thickness), and the applicability of this glass-glass fusion bonding technique for nanofluidic channels has never been tested.

4.2 Fabrication process

We used the same pattern for the anodic bonding characterization (Chapter 3) to test the feasibility of using the fusion bonding technique for fabricating sub-100-nm thick channels. The fabrication process used in this research is shown in Figure 4.1, described as follows.

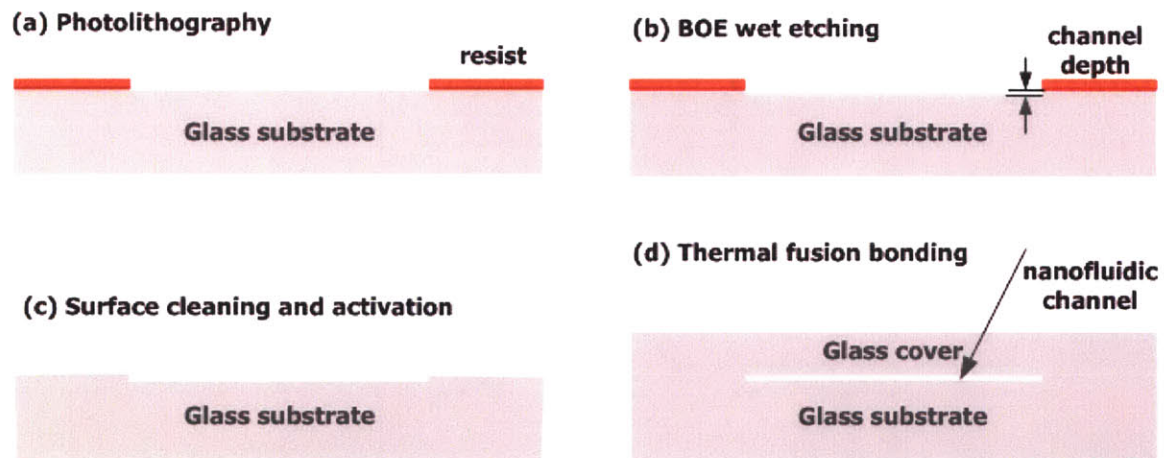


Figure 4.1 Schematic of fabrication process of nanofluidic channels on glass substrate.

Photolithography: Borosilicate glass wafers (PYREX or Borofloat, Sensor Prep Services, Inc.) were cleaned in a piranha solution (H_2SO_4 (%): H_2O_2 (%) =3:1) for 10 min, rinsed in DI water and spun dry with nitrogen gas. The dehydration process was performed by baking the glass wafers at 120 °C for more than one hour in a convection oven. To improve the adhesion of the photoresist, the wafers were then vapor primed with HMDS oven. The primer-treated substrates were coated with an OCG 825 positive resist, and soft baked at 95 °C for half an hour in a convection oven. The wafers were exposed by UV contact lithography. The exposure dose was increased a little, compared to the silicon substrate, because of the transparent glass substrate. The exposed wafer was developed for 1 min with the developer OCG 934 1:1. After rinsing in DI water and blowing dry, the hardbake process was carried out at 120 °C for 30 min in an oven. Finally, the resist layer thickness measured with surface profilometer was about 1.2 μm , which can provide an enough long survival time of resist in the BOE etchant to achieve up to 300 nm deep channels.

Glass Etching: The glass substrate was immersed in a commercial buffered oxide etch (BOE 7:1) without agitation. The depth of the nanofluidic channel can be well controlled by tuning the etching time. The remaining photoresist was removed in piranha solution after BOE etching. The etched depth was measured by P10 as described in the chapter 3.

Direct Glass-glass Bonding: The etched glass substrate and another glass cover were cleaned in piranha solution for 15 min and then activated with 28% ammonium hydroxide at 50 °C for 30 min. After spinning dry, the two glass wafers were then

carefully aligned and pressed together to make a spontaneous bonding with about 5 lb weights (metal plate) placed on the top for a couple of hours or overnight prior to the thermal bonding process. Then annealing was performed without pressurized weights by fusing the two glass wafers in a programmable furnace (Model BF51894C-1, Lindberg/Blue M, NC) at 550 °C for 12~15 hours with a ramp rate of 1.5 °C min⁻¹ and a cool-down rate of 2.5 °C min⁻¹.

4.3 Results and discussion

4.3.1 Characterization of Device Fabrication

An evaporated metal film or polysilicon/nitride layer is usually used as a wet-chemical etch mask for fabrication of microfluidic devices on glass substrate. Instead, in this study, a thin layer of photoresist (OCG 825) was employed as an etch mask for borosilicate glass in the BOE etchant. We found that more than 300 nm deep channels could be achieved after BOE etching. A calibration of the etch rate of borosilicate glass without agitation in the commercial BOE etchant (7:1) at room temperature was done and the graph of the channel depth versus the etch time is given in Figure 4.2. It is shown that BOE etches glass very fast in a short etching time (within 1 min) and then the etch rate reaches a stable speed of 24 nm min⁻¹ over 12 min. This is most likely because borosilicate glass is a multicomponent mixture of SiO₂ and other metal oxide (Na₂O, CaO, MgO, and Fe₂O₃), the insoluble products will be present and the formation of crystalline precipitates will hinder the etching process by preventing etchants from contacting the glass substrate while etching glass in a HF-containing solution⁸⁷. This observed etch rate is much slower than 0.063 μm min⁻¹ reported by Vossen⁸⁹.

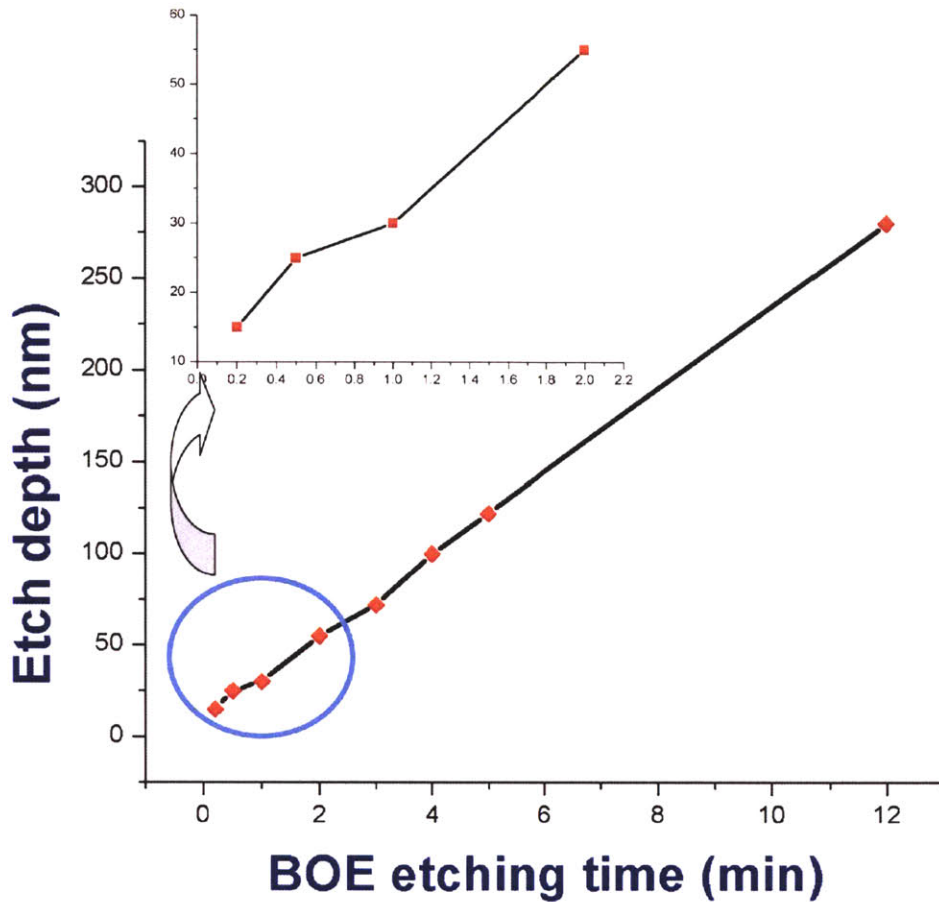


Figure 4.2 The etched depth of nanofluidic channels as a function of etching time of glass without agitation in BOE (7:1) etchant.

Here we used direct glass-glass bonding to seal the channels. The important factors affecting successful thermal fusion bonding of glass chips include the cleanness of the bonding glass surface, surface flatness of glass substrates, bonding temperature, and pressure. The glass wafers we used were double-side polished with standard tolerances (15~20 Å surface finish). The cleanness of glass substrate was achieved using hot piranha solution to remove surface contaminants, followed by hydrolyzing glass surface with boiled ammonium hydroxide. Immediately after cleaning, the two glass substrates were

brought into contact and pressurized with weights at room temperature for overnight. The applied pressure produces small deformation of the substrate to keep the two substrates sufficiently close to allow the intermolecular force to be strong enough to bond. Our experimental results support the assumption that the glass substrates might be joined by hydrogen bond formation⁸³. About 70%~80% bonded areas (6" chip area) were achieved due to this weak, reversible hydrogen bonding. Permanent bonding was done by annealing glass substrates without any pressure in a programmable furnace at high temperature with slow ramping and cooling-down rate. We found that a temperature less than 500 °C generally caused a relatively weak bonding, which could not withstand the cutting process with diamond cutter, even after annealing for quite a long time at that temperature. We chose 550 °C as the annealing temperature, which is close to the glass transition temperature (~530 °C) for Pyrex. At this temperature, a strong bonding between the two glass substrates was produced with 100% bonding yield and the bonded areas were increased to 90%-95% after heating. Although no apparatus was used to determine exact bonding strength, it was found that the bonded chips could withstand cutting and breaking process, and there was no permeation around the channel when bringing dye into the channel for leakage test even with applied high voltage of 1 kV (300 V/cm field strength). In addition, the interface between the two glass plates disappeared after the fusion bonding process. Hence, we believe that considerably strong permanent bonding between glass substrates at 550 °C has been achieved to fabricate nanofluidic glass chips. The temperature above 550 °C could accomplish stronger bonding, however, the nanofluidic channels bonded at higher temperature than 550 °C have more tendency to collapse because the glass material will be melted and deformed.

For example, Fan *et al.* found that 1-mm- wide channels made of Pyrex at 650 °C collapsed⁸⁸. One or two days are required to fabricate the glass chips, which is allowable for most applications.

Table 4.1 Survival or collapse of the nanochannels consisting of 2 cm long parallel lines spaced by 5 μm after direct glass-glass bonding

Depth	Channel width						Maximum aspect ratio
	1 μm	3 μm	10 μm	20 μm	50 μm	100 μm	
100nm	Survive	Survive	Survive	Survive	Survive	Survive	1000
55nm	Survive	Survive	Survive	Survive	Survive	Survive	1820
25nm	Survive	Survive	Survive	Survive	Survive	Collapse	2000
15nm	Survive	Collapse	Collapse	Collapse	Collapse	Collapse	67

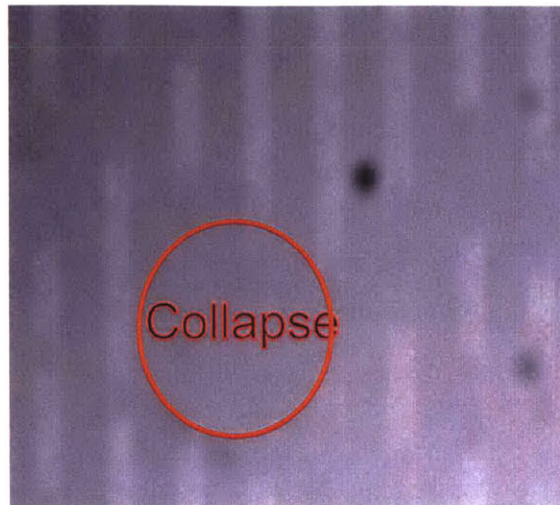
Bonding Condition: Pyrex glass (6", 500 μm thick, double side polished); 550 °C; no pressure; Programmable box furnace.

In addition, the capability and limit of this technique for the fabrication of nanofluidic devices on glass substrate has been systematically investigated. Table 4.1 summarizes the results of bonded channels with various widths and depths by optical inspection. Nanochannels as deep as 25 nm on glass substrate with high aspect ratio of 2000 have been achieved reliably. Figure 4.3 (A) shows the optical image of 25 nm deep channels. This aspect ratio is much larger than the one (~250) obtained for silicon-glass channels by using anodic bonding technique. In addition, we succeeded in pushing the thickness of nanochannels down to 15 nm, but a low aspect ratio of 67 was required to fabricate non-

collapsing channels. We attributed this failure to the roughness of both HF-etched surface and material surface finish. The optical image of the 15 nm deep nanochannel with a width of 3 μm is shown in figure 4.3 (B). It can be seen that nanochannels collapsed in some regions but survived in the other regions, which is different from the collapsing phenomenon in the silicon-based nanochannels where the channels completely collapse except along the edge (Figure 3.3). This is probably because we are not exerting strong external force to push the two interface together as in anodic bonding. While this allows larger aspect ratio channel to be fabricated, the weak bonding force decreases the bonding yield slightly (~95% bonded surface instead of ~100% bonded surface in anodic bonding).



(A)



(B)



(C)

Figure 4.3 Optical micrograph of glass nanochannels. (A) 10 μm wide and 25 nm deep nanochannels survived after bonding. (B) 3 μm wide and 15 nm deep nanofluidic channels collapsed. (C) Fluorescence imaging of 30 nm deep glass fluidic channels, 30 μm in width, being filled with 20 μM Alexa Fluoro 488-labeled 18-mer DNA oligos in TBE 5X buffer solution.

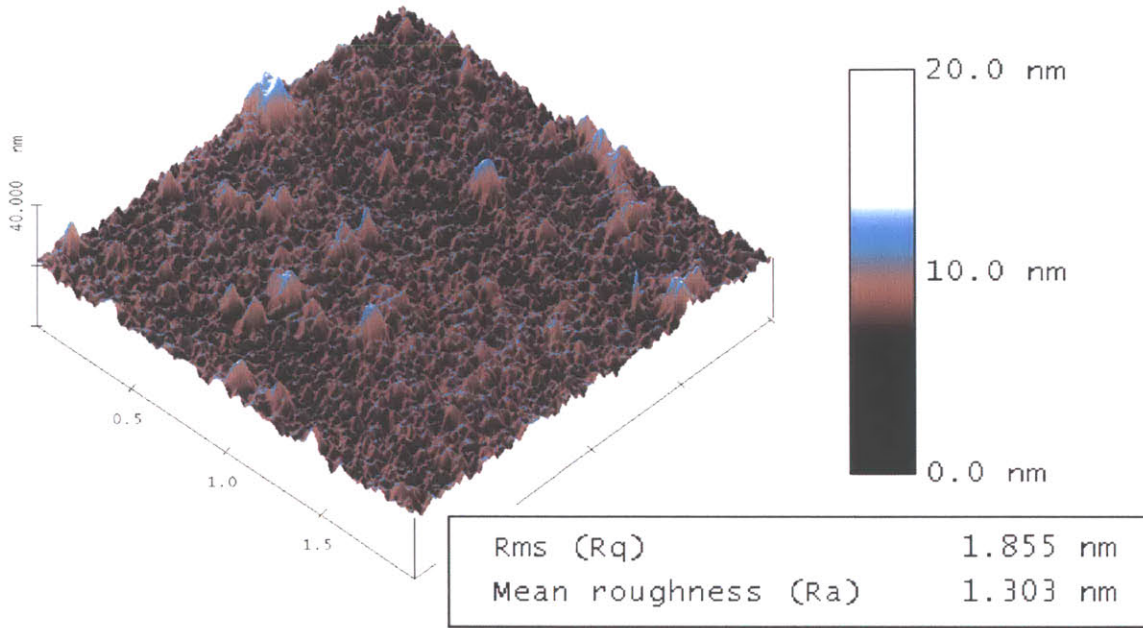


Figure 4.4 Surface profile of a glass channel etched for 30 sec in BOE (7:1) without agitation, using atomic force microscopy. The surface roughness is around 1.3 nm.

The main reason for failure in this case, seems to be the roughness of substrate surface. Figure 4.4 shows the surface profile of an etched glass channel in buffed HF for 30 sec by using an atomic force microscope (Nanoscope III, Digital Instrument). The average surface roughness (R_a) is around 1.3 nm inside a $2.0 \times 2.0 \mu\text{m}^2$ scanned area, which is comparable to the original surface flatness (guaranteed by the manufacturer) of glass material we used. Therefore, the short etching process did not increase (local) surface roughness significantly. Given the pattern of collapsed regions in the 15 nm nanochannel fabrication, it is more likely that the long range thickness variation of the glass substrate might have caused the failure shown in Figure 4.3 (B). Due to the specification of the Pyrex glass material and surface roughness resulted from wet etching process, we believe

that 20 nm would be the minimum thickness to be achieved with this fabrication technique for a wide range of aspect ratio.

4.3.2 Depth Measurement after Thermal Fusion Bonding

Due to the potential flow of glass material at high bonding temperature, the actual thickness of nanochannels after bonding might be different from the thickness measured by surface profilometer before bonding. This is especially so since the bonding temperature is close to the glass transition temperature of the Pyrex glass. SEM imaging was performed to investigate this issue. The cross-sectional SEM images of nanochannels with various depths are shown in Figure 4.3. It was shown that the etched channels were completely open and retained their original shape with good uniformity, and even the undercut from wet etching process can be observed. In addition, no interface was visible between the two glass substrates. Also, it was found out that the thickness of the channels measured by SEM imaging after bonding was almost equal to the thickness before bonding, within 10% error inherently caused by a profilometer or SEM image analysis. Hence, we demonstrate that there is no significant change of the depth due to the fusion bonding process at 550 °C.

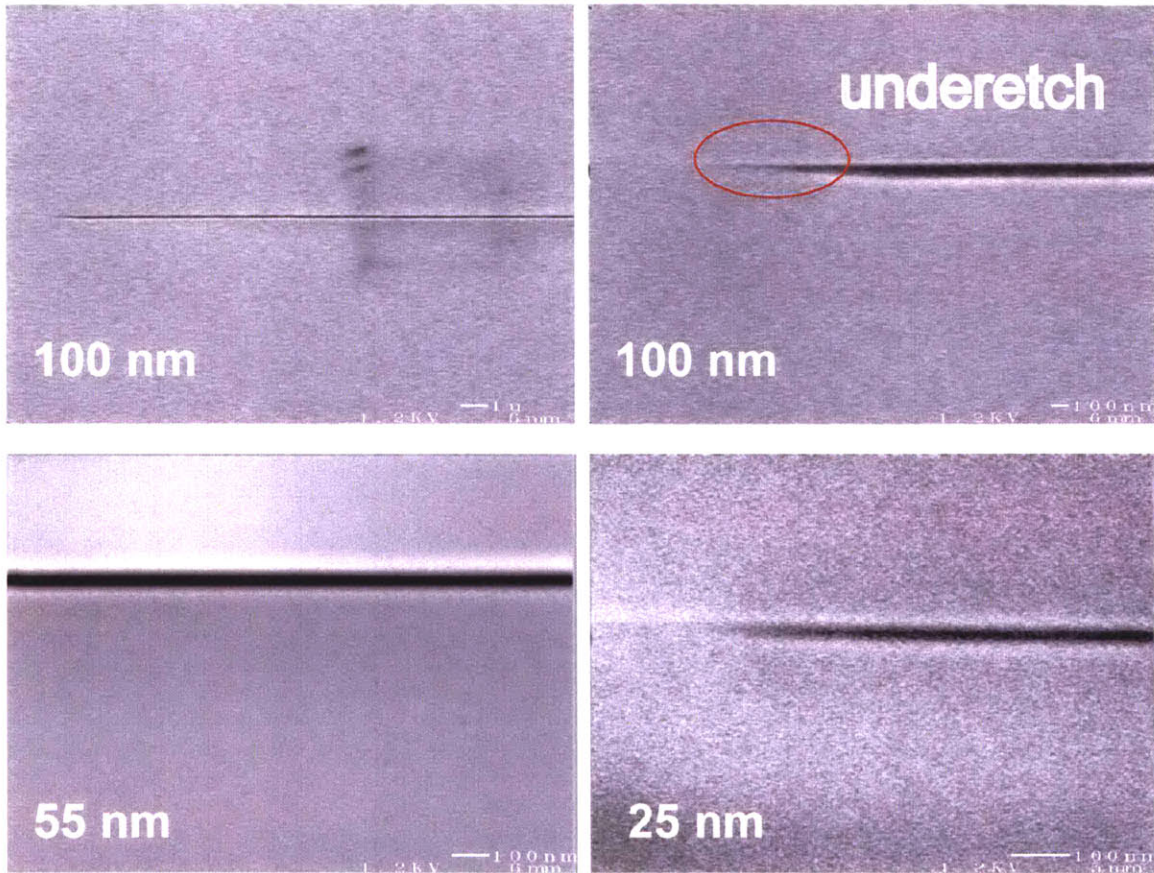


Figure 4.5 Cross-sectional SEM images of nanochannels with the depth of 100 nm, 55 nm and 25 nm fabricated on glass substrate bonded with another glass cover.

4.4 Conclusions

We have fully characterized a glass-glass fusion bonding process at high temperature for the fabrication of uniform, flat sub-100-nm nanofluidic channels. We demonstrated that nanochannels as thin as 25 nm, with aspect ratio as large as 2000, can be fabricated in the bonding temperature of 550 °C. Cross-sectional SEM analysis proved that there is no significant change of the depth of the nanochannel observed, before and after the glass-glass direct bonding process. This bonding method also provides the possibility of

fabricating nanofluidic channels on other types of glass substrates. For example, it might be used for fusion bonding of two fused silica substrates or two silicon substrates with an oxide layer (like native oxide or SOI device).

The transparency of the channels makes them a very good candidate for the applications associated with sensitive optical detection. The problem of excessive optical background signal encountered in FCS experiment with silicon-glass nanochannels, as mentioned in the last chapter, can be circumvented with glass channels. Also, the availability of such a uniform, flat nanofluidic channel provides an ideal platform for more careful, controlled study of molecular and fluidic transport in nanopores or confined space. This result will be useful in designing next-generation nanofluidic devices that can be used for protein separation⁴⁰ and biomolecule preconcentration⁹⁰.

One of the issues with this planar nanofluidic channel, however, is that the conductance of the channel is limited, compared with nanoporous materials (gels) for biological applications such as biomolecular separation. Nanochannels with large conductance would be in great demand for higher mass-throughput molecular analysis, which will be discussed in the next chapter.

Chapter 5 Fabrication of Vertical Nanofluidic Channels by Anisotropic Etching of Silicon

While the pore size of the nanofluidic channels can be precisely controlled as described in the previous chapters, the overall (fluidic) conductance of the channels is quite limited compared with nanoporous materials such as gel. Massively-parallel nanofluidic channels or filters, with fluidic conductance as large as standard microfluidic channels, would be highly desirable for efficient molecular separation and manipulation applications. This chapter describes a novel fabrication strategy for generating MEMS based nanofilters with both well-defined pore sizes and large fluid and molecular conductance. This technique is also based on photolithography and therefore relatively inexpensive, and one can integrate an arbitrary number of filters in series or parallel, using a combination of deep reactive ion etching (DRIE) and anisotropic KOH etching followed by an oxidation step. The lateral nanofilter array device achieved separation of the mixture of λ -DNA and Hind III digest of lambda DNA in half an hour with a separation distance of 1.8 cm, which could be explained by the mechanism of entropic trapping^{25, 37, 38, 64}. The fabrication strategy for the nanofilter array device has to be further optimized to achieve a uniform gap size and decrease in filter gap size. This fabrication strategy could be a key to high-throughput nanofluidic sample-preparation microsystems.

5.1 Background

Fluidic structures with the critical dimension down to 100 nm are important for advanced molecular control. In Chapter 3 and 4, thin nanochannels have been fabricated reliably and inexpensively with the critical dimension (channel depth) down to the 20 nm level. However, there is one problem with this “thin” nanochannel strategy, which is the limitation of the throughput. While the thin nanochannels are a good model system for studying molecular dynamics in confined spaces^{46, 47, 50, 62}, and have achieved great success in biomolecular separation^{25, 40}, higher fluidic conductance would be preferred for the applications of high-throughput molecular sorting, filtration and separation. One approach is to generate deep massively-parallel vertical trenches with the narrow width precisely controlled below 100 nm.

Anisotropic etching is one of the oldest techniques used in silicon micromachining and MEMS. The etch rate of silicon in some aqueous etchants such as potassium hydroxide (KOH), tetramethyl ammonium hydroxide (TMAH) and ethylenediamine based solutions (EDP) greatly depends on the crystallographic orientation of the etched surface. Etching of (111) crystallographic planes is extremely slow compared with other planes. Anisotropic etching of (110) silicon provides an attractive and effective method for fabrication of high-aspect-ratio structures with smooth and vertical sidewalls because of the high selectivity between (110) and (111) planes (larger than 100:1)⁹¹⁻⁹³. The ability to etch high-aspect-ratio structures with high precision offers numerous possibilities of technological application including the fabrication of sensors and actuators^{92, 94}. For example, Kendall used this technique for generating very narrow (0.6 μm wide), deep ($\sim 44 \mu\text{m}$) trenches on Si wafers, already in 1975⁹¹. However, the traditional

photolithography even with projection lithography is limited to pattern lateral structures below 300 nm. Although electron beam lithography (EBL) is believed to have the resolution limit of about 10 nm, it would be highly expensive and challenging. In addition, the slow etching (111) plane (undercut) deteriorates the efforts of achieving the smallest lateral thickness possible down to 100 nm.

We developed a novel fabrication strategy for generating nanofluidic filters with the controlled critical dimension (lateral gap thickness) between 10 nm and 500 nm for molecular sorting and manipulation applications. We used anisotropic KOH etching of (110) silicon or a combination of deep reactive ion etching (DRIE) and anisotropic KOH etching to achieve arbitrary deep trenches with flat and smooth wall surface, which is important for the pore size control of the nanofluidic filter. Thermal oxidation takes place at silicon-silicon dioxide interface and original wafer will be thickened as the silicon oxide layer is formed. Hence, a thermal oxide layer can be grown to narrow the lateral gap (made by anisotropic etching of Si) width down to the desired size, possibly down to 10 nm. This fabrication process is inexpensive, simple and can be well controlled. This could be a fabrication strategy for massively parallel, regular nanopore or nanofilter systems^{95, 96}, but with much better control over pore size and geometry, as well as fabrication flexibility. Potential applications include high-throughput biomolecule separation and analysis as a replacement of capillary electrophoresis (CE), novel biomolecular filters for desalting, and advanced biomolecule filters for preconcentration of biomolecules, and advanced fluid and molecular transport control such as in drug delivery.

5.2 Experimental Methods

5.2.1 Fabrication Technique

Precise alignment of the features to the true (111) planes is of critical importance for achieving high-aspect-ratio structures. It has been confirmed by previous researchers that precise alignment within 0.1 degree is required to obtain high anisotropy ratio in KOH⁹¹⁻⁹⁴. This requirement is an order of magnitude smaller than the accuracy of the major flat of commercially available (110) silicon wafers, which is typically 2 degrees. We used both a fan-shaped pattern and a diamond shaped window, reported by Uenishi *et al.*⁹² and Hölke *et al.*⁹³, respectively, for finding the minimum underetch of the (111) planes, as shown in Figure 5.1. For fan-shaped alignment pattern, the (111) planes could be determined by examining the narrowest line after the wet etching, where minimum underetching took place (Figure 5.1 A). The diamond-shaped window was etched anisotropically, until it ended up with a hexagon bounded by the (111) planes (shown in Figure 5.1 B). Although the resulting left and right sides of the etched window are not perfectly aligned on the same plane but has a small angle, the pattern aligned between the two lines will then underetch with the smallest possible rate (therefore the (111) plane).

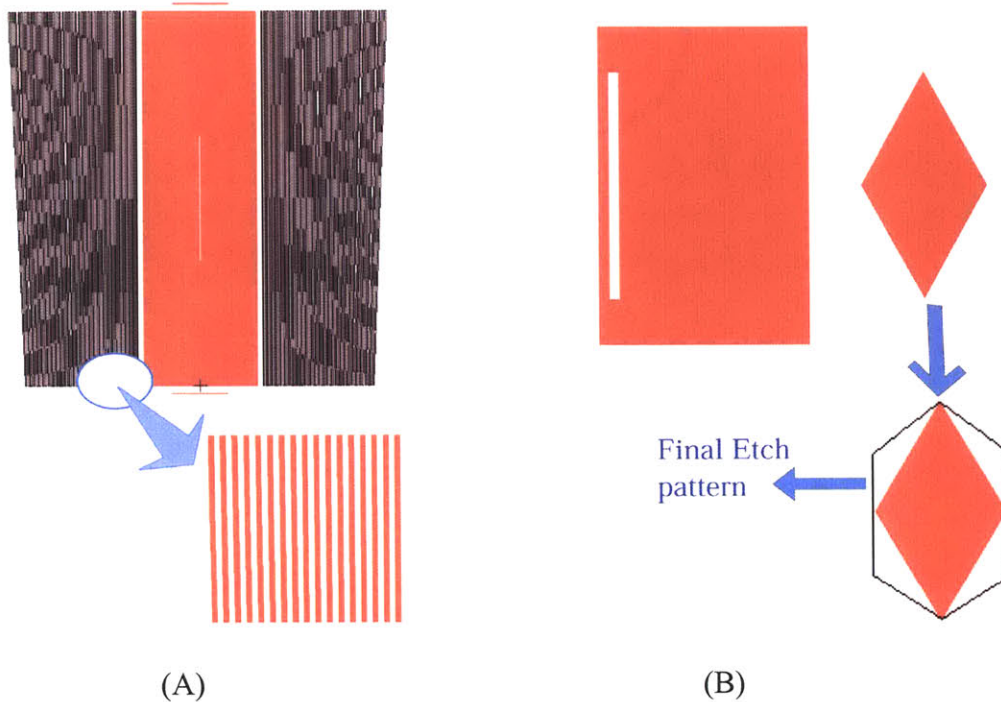


Figure 5.1 Alignment marks for determining the minimum underetch of the Si (111) planes. **(A)** A fan-shaped pattern consists of 3 mm long and 10 μm wide lines spaced by 10 μm, which fan out at 0.05 degree angles to one another and span from -2 degrees to 2 degrees. **(B)** The final etch pattern of the diamond shaped window is defined by the intersection of (111) planes.

The overall fabrication process for generating massively parallel, vertical nanofilters is outlined in Figure 5.2 (A) and (B). Commercial p-type Czochralski grown 6" (110) wafers with a resistivity of 10-20 Ω cm and a thickness of 625 μm were used (El-CAT, Inc., NJ). First, a thin layer of silicon nitride was deposited on (110) silicon substrate by LPCVD to provide an etch mask for KOH etching. The fan-shaped and diamond-shaped alignment mark for determining the direction of (111) planes within 0.1 degree were patterned and etched in aqueous KOH solution to a depth of 10 μm. Then channels with

various gap sizes were defined and etched by standard photolithography and anisotropic KOH etching. The features in this step were aligned to the (111) planes of silicon. The etch rate of (110) plane in 40 wt% KOH is around $0.7 \mu\text{m}\cdot\text{min}^{-1}$ at 70 °C. Alternatively deep reactive ion etching (DRIE) technique was used to achieve deep trench etch with Bosch process, and the etch depth could be made larger than 100 μm . Although deep reactive ion etch of silicon provides high-aspect-ratio etching and anisotropic etching capabilities, the sidewall will become rough and have scallops with the order of 100 nm. Hence a short period of KOH dipping was performed to smooth the “rough” walls. After KOH etching, all the walls will end up with smooth (111) planes. After removing the silicon nitride layer, scanning electron microscopy (SEM) or optical microscopy was used to measure the gap size in order to determine the desired oxide thickness. Based on the gap size, an oxide layer with appropriate thickness is grown to narrow the gap down to ~100 nm. Finally, the silicon device was bonded to a flat glass plate by anodic bonding or thermal fusion bonding technique.

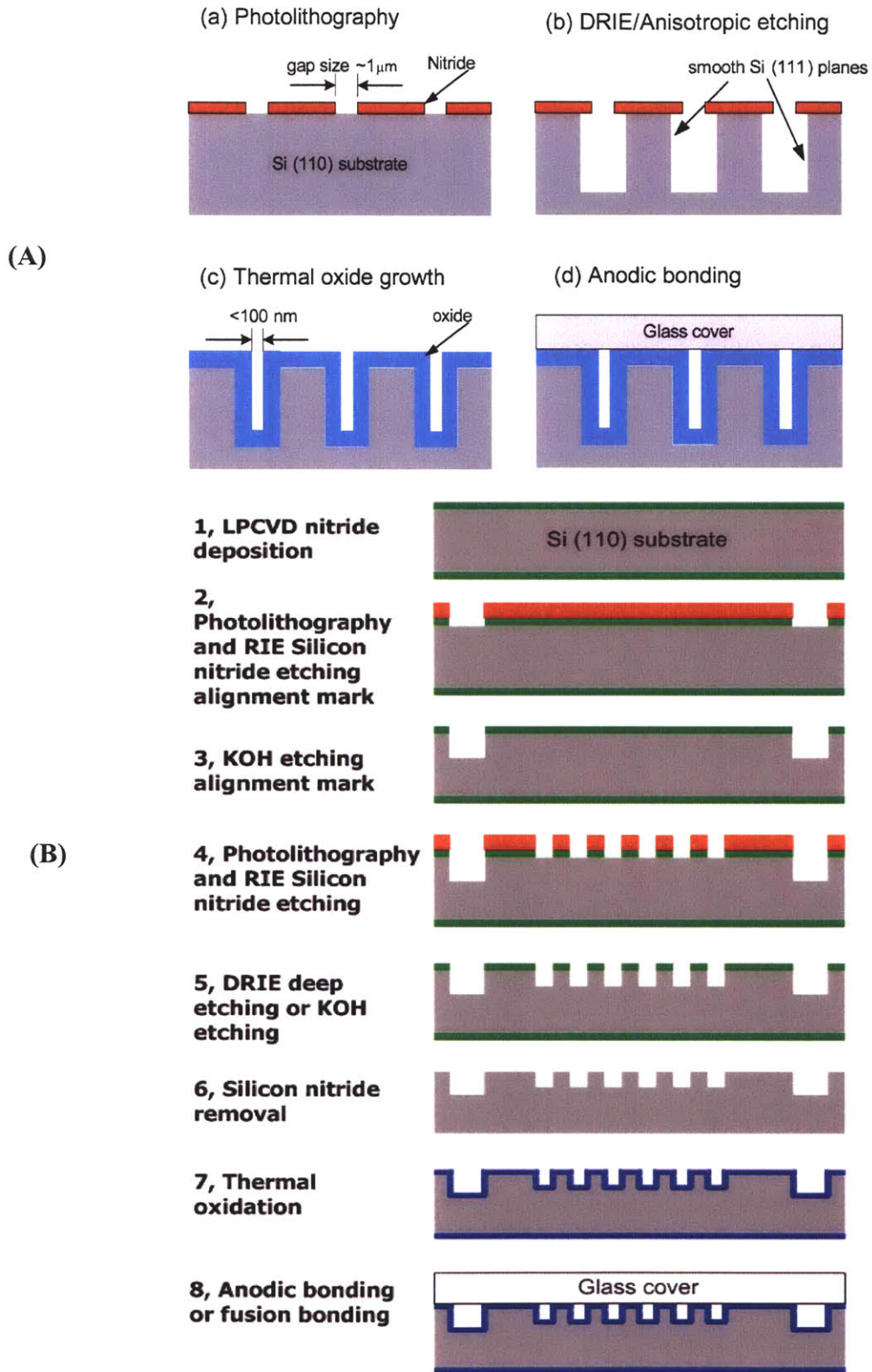


Figure 5.2 (A) Outline of generating lateral nanofluidic filters (top view). (B) Fabrication process of vertical nanofluidic filters with DRIE/anisotropic etching.

5.2.2 Sample, Electrophoresis condition, and Microscopy

λ -DNA and Hind III digest of lambda DNA (New England BioLabs, MA) were stained with the intercalating fluorescence dye YOYO-1 (Molecular Probes) at a ratio of 1 dye to 10 base pairs in a buffer of 5X Tris-Borate-EDTA (TBE) and 0.1M DTT. After mixing of λ -DNA and Hind III digest of lambda DNA, the final DNA concentration was approximately 60 $\mu\text{g/ml}$. The device was first completely filled with 0.5X TBE buffer with the help of inducing an electroosmotic flow between two reservoirs. Then the buffer solution was replaced with 5X TBE buffer. An inverted epi-fluorescence microscope (IX-71, Olympus, Melville, NY) equipped with a thermoelectrically cooled CCD camera (Sensicam QE, Cooke Co., Auburn Hill, MI) was used for fluorescence measurement. A 10X microscope objective lens was used for imaging DNA molecules and acquiring electropherogram.

5.3 Results and Discussion

5.3.1 Fabrication Characterization

(1) KOH etching ONLY

Anisotropic etching of (110) silicon substrate allows us to produce narrow and deep trenches. 7 μm deep trenches with a width of 1.5 μm , made by anisotropic etching for 10 min in 40 wt% KOH at 70 $^{\circ}\text{C}$, were narrowed down to 400 nm after growing an oxide of 1.05 μm , as shown in Figure 5.3. A uniform and vertical trench array with smooth sidewall was achieved and we believe that the width of narrow trenches could be decreased to 100 nm or below with a thicker oxide grown. KOH etching proved to be effective for forming slot structures (parallel lines), but fails to generate rectangular

"pillar" structures because the hexagonal shapes form after KOH etching as shown in Figure 5.1 (B). The four (111) crystal planes intersect the (110) surface plane while the other two (110) planes intersect the (110) surface plane at an angle of 35.3° . Our experiment demonstrated that the rectangular pillar structures were etched away within 2 min in KOH solution. Also, the maximum depth in KOH etching ultra-deep and narrow structures will be limited⁹³.

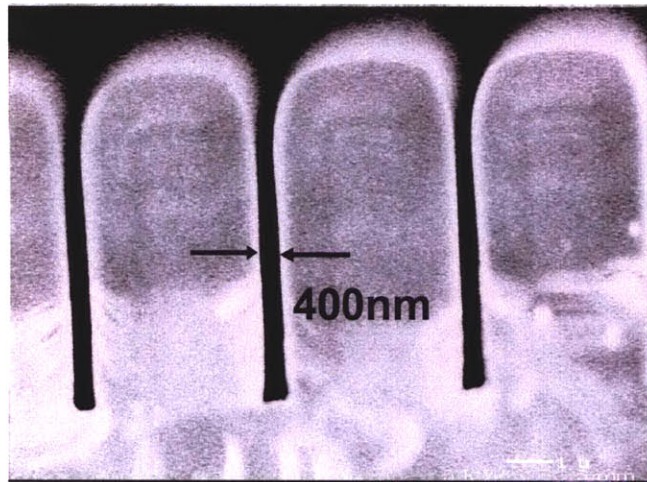


Figure 5.3 Cross-sectional SEM micrograph of a trench array. Long vertical slot structures were achieved by KOH etching for 10 min. The trench width (gap size), which is uniform, was 400 nm after a silicon oxide of $1.05\ \mu\text{m}$ was thermally grown.

(2) Combination of DRIE and KOH etching

Alternatively, we used the combination of DRIE and KOH etching to fabricate high-aspect-ratio vertical trenches. The conventional deep silicon reactive ion etching (DRIE) can be done to define very deep trenches, and then the rough sidewalls can be ‘smoothened’ by a short anisotropic KOH etching as described above. KOH etching time

has to be well controlled and characterized to make sure all the scallops or rough sidewalls caused by DRIE etching are smoothed out. As can be seen in Figure 5.4, 2 min KOH etching allowed us to generate uniform deep trenches (Fig 5.4 A), while tapered trenches were produced with only 30 sec KOH etching (Fig 5.4 B). Hence, 30 sec of KOH etching time is not long enough to achieve vertical walls. However, 2 min KOH etching required to generate a smooth surface deteriorates the hope of generating rectangular pillar structures because it will kill all the pillar structures as described above. Therefore, we need and might be able to do better DRIE with smoother sidewalls, as a result of less KOH etching time required, by controlling etch parameters. In fact, however, the narrowness of these trenches is greatly limited by the DRIE step. Too narrow a trench will create a tapered profile, and also a rough sidewall⁹⁷. Therefore, in some sense, DRIE capability of generating vertical deep trenches is impaired when etching the trenches with very narrow gap ($\sim 1 \mu\text{m}$).

In addition, a grown oxide as thick as $1.5 \mu\text{m}$ after 30 sec KOH etching, achieving the minimal gap size down to 120 nm, did not reduce the nonuniformity of the gap size of the etched trench, as shown in Figure 5.4 (C). Although it is believed that the oxidation of high-aspect-ratio structures is affected by oxidation retardation⁵, uniform oxide shown here demonstrates the possibility of narrowing down the gap size uniformly by thermal oxidation.

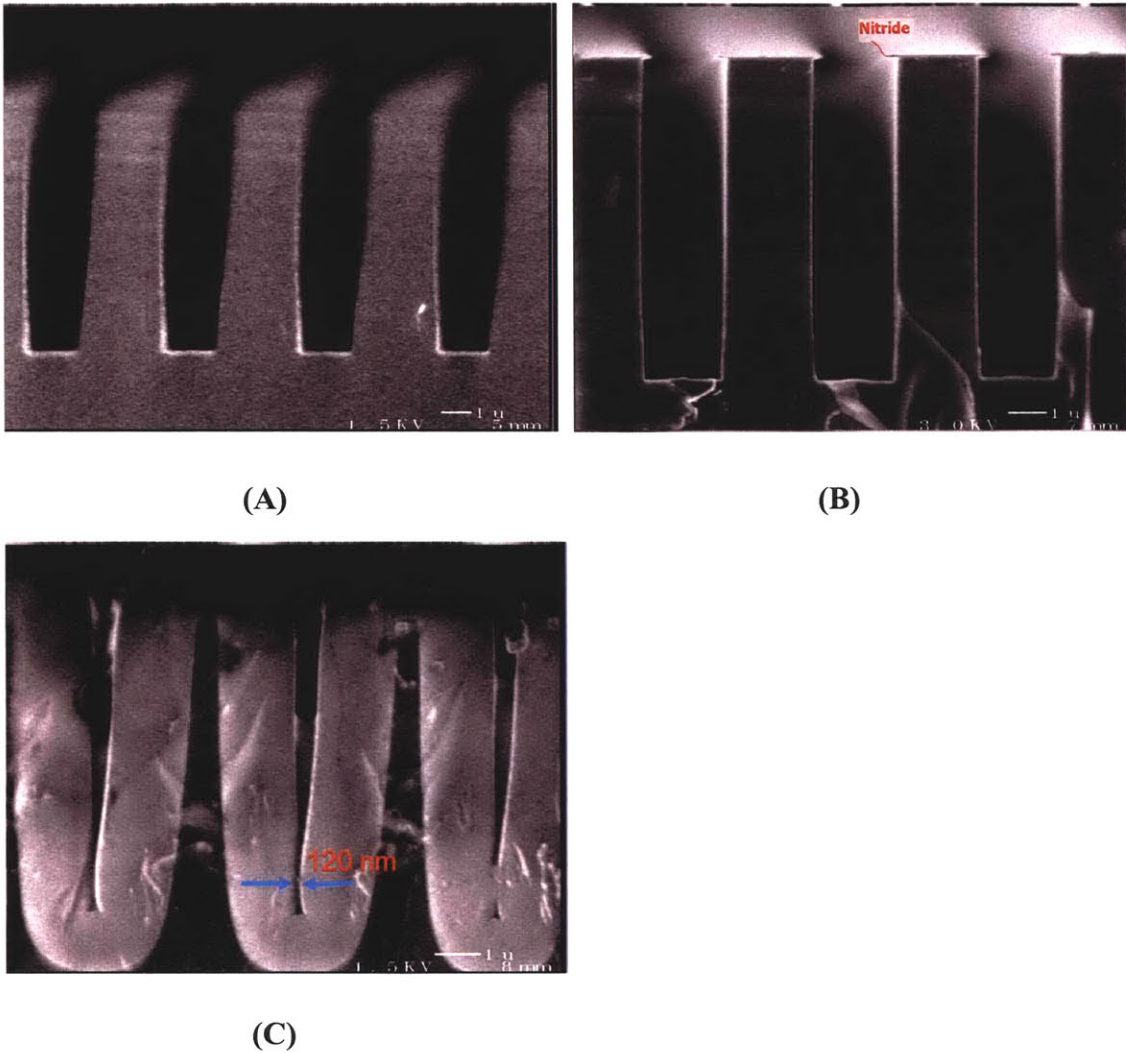


Figure 5.4 Cross-sectional SEM images of narrow and deep trenches after a combination of DRIE and KOH etching. The depth of the trenches was about 7 μm . **(A)** **(B)** Comparison of KOH etching time on smoothing the rough sidewalls caused by DRIE etching. Vertical slots with the uniform gap size were achieved after KOH etching for 2 min **(A)**, while tapered trenches were produced with 30 sec KOH etching **(B)**. **(C)** Tapered trenches were fabricated by using DRIE etching for 30 min followed by KOH etching for 30 sec and then growing a 1.5 μm oxide. The smallest gap size was 120 nm.

Therefore, we need a better fabrication strategy of defining and making lateral filter (narrow-region / wide-region) structures with uniform gap sizes. One approach is to combine DRIE and KOH etching by first defining narrow regions, consisting of parallel lines with a width of 500 nm to 1 μm , with anisotropic KOH etching. Then another mask layer for wide regions, which also consist of parallel lines with a width of several microns but in the orthogonal direction to narrow-region patterns, will be used. Wide regions will form by DRIE etching with rather smooth sidewalls because of the wide gap size (larger than 2 μm). If needed, however, KOH etching can be followed to achieve vertical sidewalls, which will not affect narrow-region patterns. This technique will allow us to make well- defined rectangular pillar structures, which will be used for the future work.

Another potential approach is based on macropore micromachining. Anodic dissolution of silicon is well known as a technique of porous silicon formation or for electro-polishing of silicon wafers^{10, 98-100}. The electrochemical dissolution of silicon in HF can form deep macropores with a very smooth surface in an n-type silicon substrate as described by Lehmann⁹⁸. Ohji *et al.* made cylindrical pillar structures with a submicron space by electrochemical etching in HF²⁹. The advantages of feasible aspect ratios up to 250 and remarkable straightness of pore walls allow to form massively-parallel filters, which might be investigated in the future.

5.3.2 Separation of Long DNA Molecules

As shown in Figure 5.5, a lateral entropic nanofilter array, which consists of alternating narrow and wide regions with the depth as large as 8 μm , were fabricated for separation

of long DNA molecules by using a combination of deep reactive ion etching (DRIE) and anisotropic KOH etching. The cross-sectional SEM image of the narrow regions of nanofilters is shown in Figure 5.6 (D). As described above, 30 sec KOH etching failed to generate vertical trenches. As a result, the nanofilters with the nonuniform gap size from 80 nm to 500 nm were achieved. The separation column consisted of hundreds of filters in parallel, 1 mm wide and 2 cm long totally. The T-shaped injector was fabricated to launch an initial sample. Figure 5.6 shows sequential fluorescence images of launching DNA mixtures. As enough and steady DNA sample was fed into the loading zone, an electrical field of 30 V/cm was applied across the separation column with zero potential in the sample, waste, and cathode reservoirs. In the meantime, the water level of both cathode and anode reservoirs was increased to produce pressure difference by adding more buffer solution. As a result, DNA molecules were driven into the separation column by the electric field while excess DNA molecules were drained to the sample or waste reservoirs by pressure.

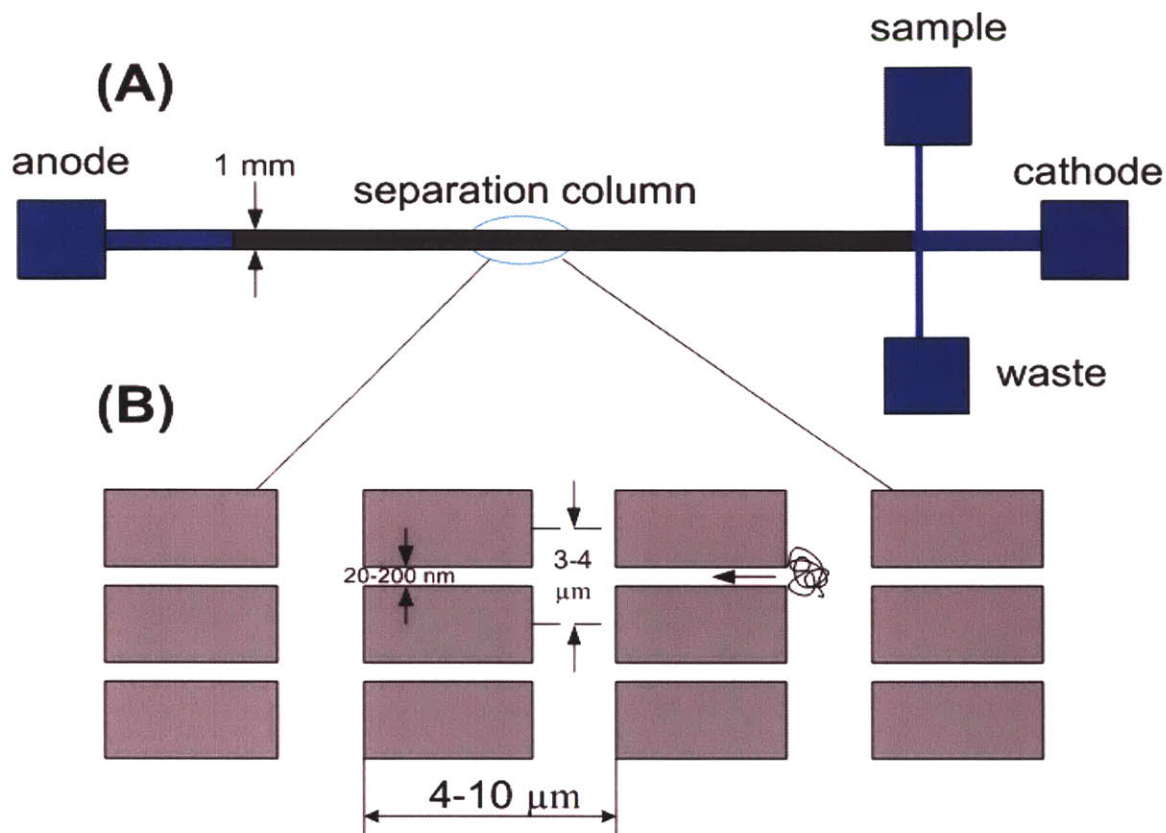


Figure 5.5 (A) Schematic diagram of the lateral nanofilter array device. The device includes four reservoirs (anode, cathode, sample and waste), a 2-cm-long and 1-mm-wide separation column and a T-shaped injector. (B) Top-view schematic picture of the periodic lateral array of nanofilters with an alternative narrow region (20~200 nm) and wide region (3~4 μm). The period of one filter was 4~10 μm and the depth was 8 μm.

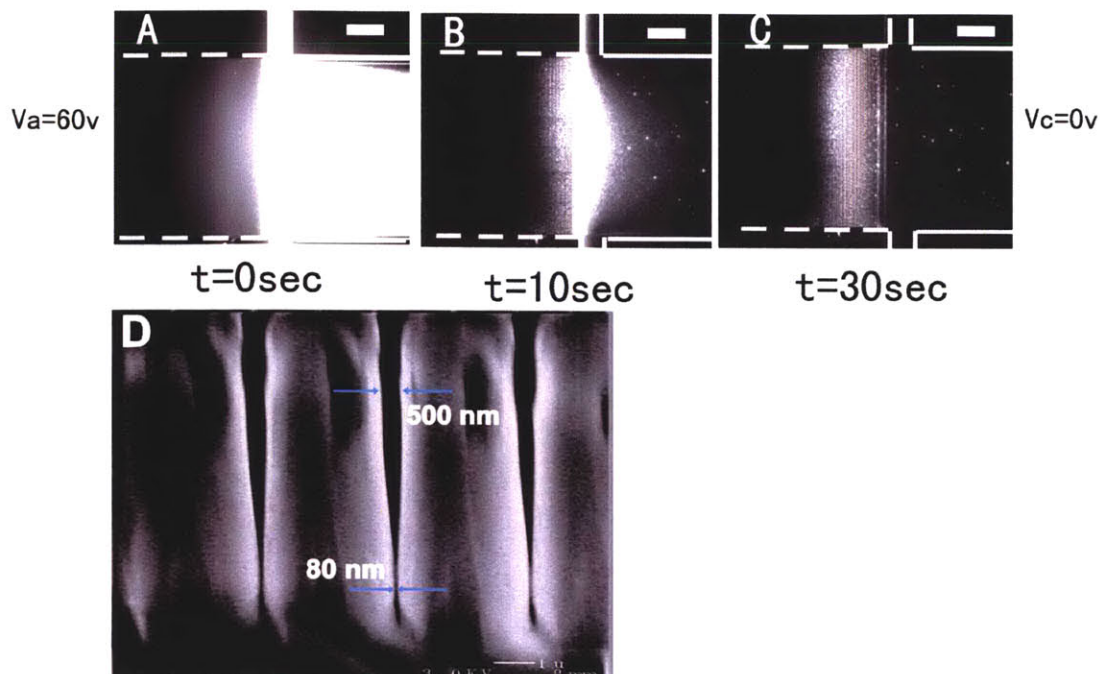


Figure 5.6 (A, B, C) Sequential fluorescence images of launching DNA samples. The dashed lines indicate the separation column and the solid lines represent the T-shaped injection channels. Molecular band was launched by applying the electrical field of 30 V/cm across the separation column and setting the water level of the anode and cathode reservoirs higher than the sample and waste reservoirs. The scale bars are 200 μm . **(D)** the cross-sectional SEM image of lateral entropic filters. The nanofilters were fabricated by DRIE etching for 35 min and KOH etching for 30 sec followed by growing a 1.5 μm thick oxide. The nonuniform gap size from 80 nm to 500 nm was achieved.

When DNA molecules were launched into the separation channel, they migrated at different speeds according to their molecule weights. The mixture of λ -DNA and λ -DNA digested by Hind III was separated at 1.8 cm below from the nanofilter entrance in around 30 min as shown in Figure 5.7. Peak assignment was identified based on the peak

height and by direct optical observation. Relative intensity change of the peak 48.5 kbp and 23 kbp, as shown in Figure 5.7 (A), might be due to insufficient mixing and loading of DNA samples. It was found that long DNA molecules moved faster than shorter DNA ones in our lateral filter device, which could be explained by the mechanism of entropic barrier transport by Han⁶, where it was described that DNA molecules overcome the entropic barrier by stretching the monomers into the constriction and the energy barrier for DNA escape is independent of the chain length. Also, it was shown that separation resolution depended on the applied electrical field. Separation resolution was improved as the electrical field was decreased and this dependence of mobility on field strength was clearer for larger molecules. For instance, 48.5 kbp and 23 kbp (peak a and b in Fig 5.7 (A)) could not be completely resolved under the field of 30 V/cm. In this run, the shortest two fragments (2.3 kbp and 2 kbp) were missing. It might be mainly because of the nonuniform gap size at the narrow constriction. The gap size more than 200 nm in some regions is larger than the radius of gyration of these two fragments (~ 100 nm)¹⁰¹, so that the effect of entropic barrier transport can't be applied in this regime. Also, the amount of launched DNA molecules of these two fragments is extremely small, compared to the number of 23 kbp DNA, so that our CCD could not detect such a weak fluorescence signal. However, our nanofilter system clearly illustrated the potential for separation of large DNA molecules, although it still needs to be optimized in the future.

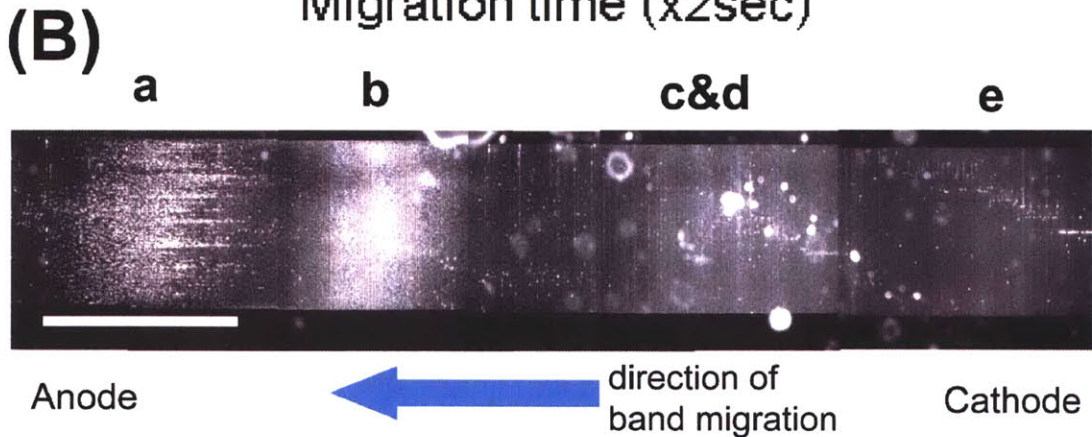
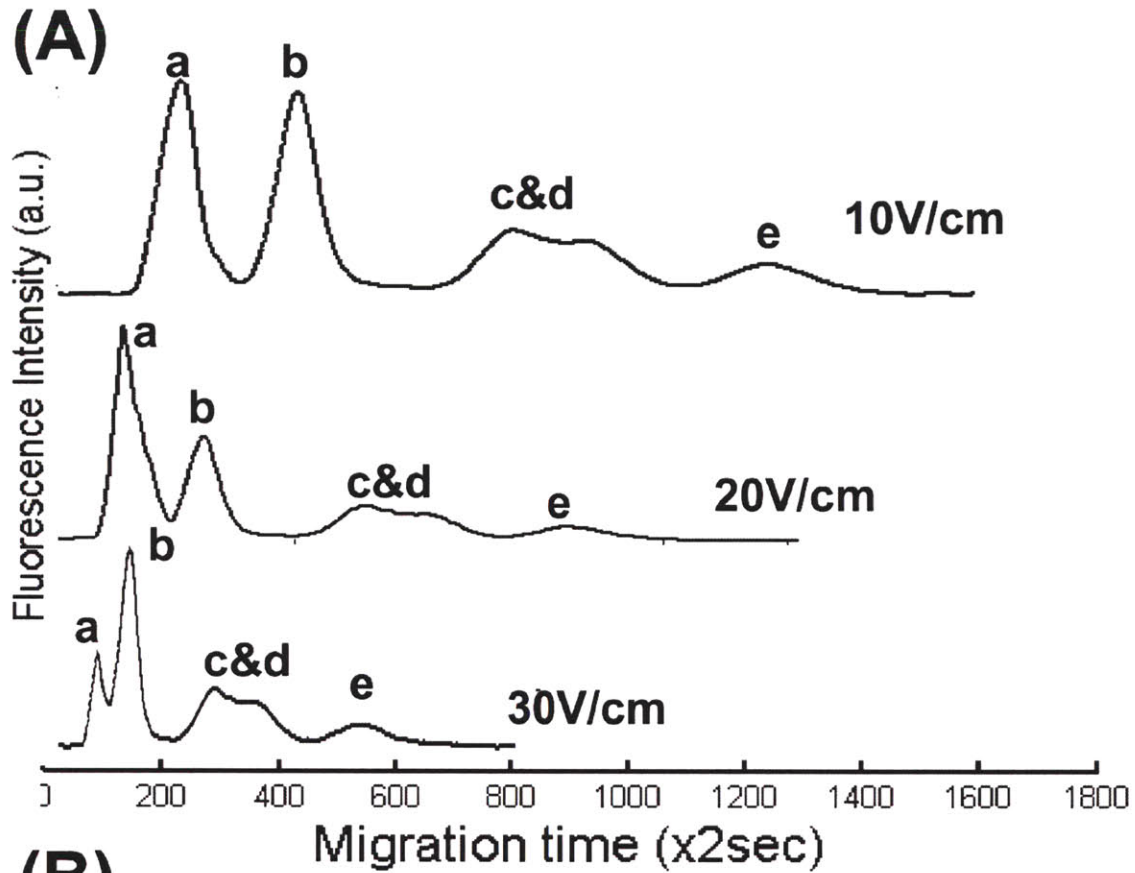


Figure 5.7 Separation of the mixture of λ -DNA and λ -DNA digested by Hind III. Peak assignment: (a) 48,502 bp, (b) 23,130 bp, (c) 9,416 bp, (d) 6,557 bp, (e) 4,361 bp. The shortest fragments (2,3 kbp and 2 kbp) were missing. **(A)** Separation of DNA mixtures under different applied electrical fields. Electropherogram was detected at 1.8 cm from the entrance of the separation column. **(B)** Fluorescence images of the DNA bands separated at 10 V/cm. A 10X objective lens was used here. The scale bar is 1 mm.

Our separation system is similar to the nanofluidic channel with entropic traps for separation of large DNA molecules developed by Han *et al.*²⁵. However, with all the advantage of the molecular filters⁶, this new molecular filters can process much larger volume of sample liquid. Our fabrication strategy could provide a way to integrate single and many (presumably more than 1,000) regular nanofilters without repeated, extensive processing. Our system can greatly improve the throughput of separation of biomolecules due to a large number of filters integrated. Direct observation of bands, just as in conventional slab gel electrophoresis, is possible even with relatively low N.A. optics (10X objective lens, see Figure 5.7 B). The detection of the sample molecular bands is now much easier, due to the longer path length and larger number of molecules being separated in the channel.

With these advantages mentioned above, the nanofilter system could be used to control the drug or molecular delivery, by taking advantage of hindered transport of molecules. Also, it could be used as a molecular sieve for separating and purifying proteins, DNA and carbohydrates. The increased throughput of the device will enhance the efficiency of the separation process, as well as the detection sensitivity. Furthermore, the nanofilter could be used as a membrane that allows the transport of fluid and small molecules, but restricts the transport of larger proteins and molecular complexes, in order to control the (bio)chemical reactions appropriately. The higher conductance of the nanofilter will be comparable to that of random nanoporous materials embedded in microchannel, which currently used for most applications.

5.4 Conclusions

We have proposed a novel fabrication technique to form massively-parallel vertical nanofluidic filter arrays with high fluidic conductance, by using a combination of DRIE etching and KOH etching of (110) silicon substrate. The lateral gap size of deep trenches can be further narrowed down to a desired thickness by thermal oxidation. The lateral nanofilter array device achieved separation of a mixture of λ -DNA and Hind III digest of lambda DNA in half an hour, which demonstrated the potential for high-throughput nanofluidic biomolecular separation.

Chapter 6 Summary

6.1 Thesis contributions

This thesis characterized the applicability and limitation of a number of fabrication techniques for making nanofluidic channels on PDMS, silicon and glass substrates, in an effort to establish platforms for biomolecular sieving and manipulation. The goal was to generate nanofluidic channels and push the critical dimension down to sub-100-nm regime, which is comparable to the size of a wide range of biomolecules, thus enabling advanced molecular control and manipulation. These fabrication methods and nanofluidic devices could have significant applications in nanobiotechnology, including separation of biomolecules, drug delivery, polymer dynamics, and single molecule detection.

This thesis is the first to demonstrate that silicon-glass nanofluidic channels, as thin as 20 nm with high aspect ratio (more than 250:1, width to depth), could be achieved with conventional photolithography, RIE etching, and anodic bonding techniques. We also demonstrated the feasibility of glass-glass nanofluidic channels as thin as 25 nm with aspect ratio of 2000 with developed direct glass-glass bonding technique. This thesis is also the first to demonstrate that there is no significant change of the depth of nanofluidic channels with varying depths down to 20 nm, due to anodic bonding process and glass-glass bonding process with scanning electron micrograph (SEM) analysis. The availability of these reliable, reproducible fabrication strategies for nanometer-sized fluidic structures is significant in designing next-generation nanofluidic devices to be used for protein separation⁴⁰ and biomolecular preconcentration⁹⁰.

Finally, this thesis has demonstrated that massively-parallel vertical nanofluidic filter arrays, with fluidic conductance as large as standard microfluidic channels, can be used for high-throughput molecular separation and analysis. The lateral nanofilter array device was fabricated by a combination of deep reactive ion etching (DRIE) and anisotropic KOH etching followed by an oxidation step. We demonstrated efficient separation of the mixture of λ -DNA and Hind III digest of lambda DNA in half an hour by using the mechanism of entropic trapping. The separation process is comparable to traditional gel electrophoresis. We believe that these devices could be a key to the high-throughput nanofluidic sample-preparation microsystems.

6.2 Ongoing research

These regular nanofluidic channels provide ideal experimental platforms for well-controlled, model-based study of molecular and fluidic transport process in confined environment. Now, two experiments for studying molecular dynamics confined in regular nanofluidic channels, in collaboration of Prof. Peter So in Mechanical Engineering (MIT) and Prof. Patrick Doyle in Chemical Engineering (MIT), are being conducted and described as follows.

(1) Study of Hindered Diffusion of Biomolecules with Two-Photon Fluorescence

Correlation Spectroscopy (FCS) Measurement

When the size of a solute is comparable to the pore size, the effective diffusion coefficient of a solute within a pore is usually found to be less than its value in bulk solution. This phenomenon is known as hindered or restricted diffusion. Steric exclusion

and hydrodynamic interaction are two mechanisms responsible for diffusional hindrance by small pores⁴². An understanding of hindered diffusion is important to heterogeneous catalysis, membrane separation, chromatography, and enhanced oil recovery. A number of previous studies of hindered diffusion through porous membranes have been conducted by using track-etched membranes^{41, 43-45}. Although the pore size can be well controlled within 15%, few materials and few pore geometries are available in this technique¹⁵. Also, it is difficult to modify and control its surface properties and integration with single molecule optical detection is hard. In contrast, nanofluidic channels provide unique capability in biomolecular control, as described before.

Fluorescence correlation spectroscopy (FCS), one of the single molecule detection methods, has capacity to extract information on dynamical processes from the fluctuation of fluorescence intensity^{50, 102, 103}. This fluctuation contains information about molecular stochastic motion, such as diffusion coefficient. By calculating the correlation function of the fluorescence signal from the detection volume, one can measure the diffusion coefficient of the molecules in the liquid. FCS presents unique advantages in measuring very dilute systems with high spatial resolution.

Regular nanofluidic channels with well-defined shapes and depths on two glass substrates, as developed in Chapter 4, will be used to restrict the diffusion of biomolecules. As shown in Figure 6.1, the stochastic motion of molecules will become two-dimensional progressively as the depth of the channel decreases. Also, the surface boundary layer could change the stochastic motion of charged molecules near the surface and might have different effects on positively and negatively charged molecules. Confinement of molecules within a small space could affect their stochastic motion, as

demonstrated by Lyon and Nie⁴⁸, who used a pulled glass capillary with submicron inner diameter to study the confinement effect. In this work, the simple geometry of nanofluidic channels will offer easier theoretical study and modelling of this problem.

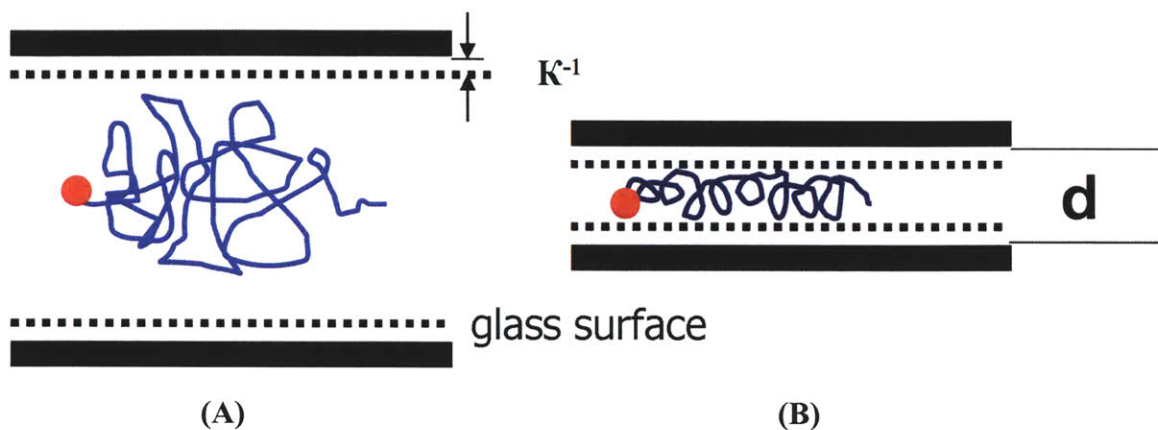


Figure 6.1 Stochastic motion (trajectories) of molecules (red spots) in a free space (A) and in a confined 2D space (B). d and K^{-1} are the channel depth and Debye layer thickness, respectively.

A new two-photon FCS setup has been built in the So lab, and will be used for the measurement of diffusion constants in the nanofluidic channel. The schematic diagram of the setup is shown in Figure 6.2. The laser light coming in from Ti-Sapphire laser will induce two-photon fluorescence excitation (frequency doubled around 400-500nm), and the resulting fluorescent light will be collected by the multichannel PMT unit, at different visible wavelengths. This two-photon method allows better rejection of excitation light (infrared) and spectral measurement of fluorescent light from the sample. Using this setup, it would be possible to measure fluorescent light from multiple fluorescent light sources that may be present in the sample, without switching the fluorescent filter combination.

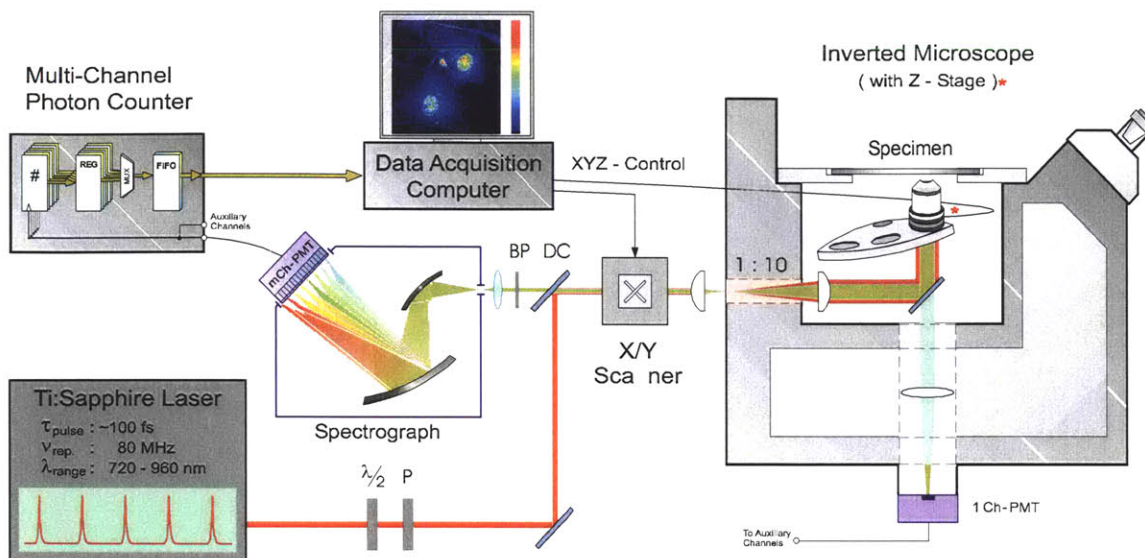


Figure 6.2 Schematic diagram of two-photon FCS setup for the measurement of diffusion coefficient in a nanofluidic channel.

The objective of this research is to investigate the changes in diffusion coefficients of molecules caused by both the existence of spatial confinement and boundary surface layer. Spatial confinement will be achieved by varying the depth (from 100 nm down to 20 nm) of the nanofluidic channels, and the thickness of Debye layer can be changed experimentally by controlling the buffer ionic strength. Here, the channel depths are still larger than the sizes of biomolecules to be used (for example, small DNA or protein). However, such nanoconstriction would still be expected to affect the stochastic motion of molecules significantly, as demonstrated in previous experiments. Also, various molecules with different shapes, charges (negatively, positively or uncharged) and mass will be investigated in such an environment. Finally, experimental data will be compared and analyzed by theoretical modelling. The potential impact of this research would be

significant both scientifically and technologically by better understanding molecular diffusion and transport in confined environment as well as generating new concepts of molecular sorting and manipulation technology.

(2) Dynamics of Genomic-Length DNA Molecules Confined in Nanochannels

The dynamics of flexible polymer in confined environments is a fundamental problem with considerable technological importance. Now the dynamics of a single, large macromolecules in confined environments can be visually monitored by fluorescence microscopy^{33, 46, 47, 101}. Recently, Chen *et al.* examined the conformation and diffusion of a single DNA molecule confined two parallel plates with both single molecule experiments and Brownian dynamics simulations⁶². However, the depth of the channel investigated was still larger than 1 μm and it is unclear how a chain molecule behaves when confined below 500 nm even down to 100 nm (close to its persistence length).

In this study, we focus on the mobility, the equilibrium conformation and the diffusion of a single DNA molecule (λ -DNA) confined in a very thin nanofluidic channel, fabricated on glass substrate, as shown in Figure 6.3. The single DNA motion will be captured and determined with an epifluorescence video microscopy in the Doyle group. The degree of chain stretching and the diffusivity will be characterized as a function of the chain confinement (the depth of the nanochannel).

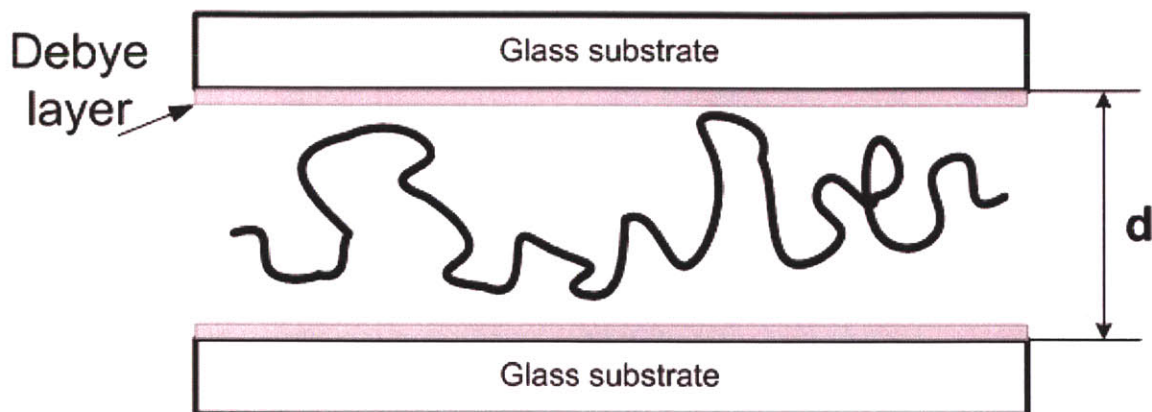


Figure 6.3 Schematic diagram of a large DNA molecule confined to a slit channel with a depth of d .

6.3 Outlook and Future Work

This thesis has explored the limit of the substrate bonding techniques, both anodic (Si-glass) and fusion (glass-glass) bonding, in fabricating sub-100-nm thick nanofluidic channels. However, It is not clear whether 20 nm is the ultimate minimum thickness that can be attained from anodic bonding technique. The attempt will be made to push the ultimate thickness down to 10 nm level. Also, bonding temperature and pressure might have effect on the success of the structure, which is to be investigated in the future. In addition, glass-glass bonding needs to be optimized to achieve better bonding yield and quality. Possible future work also includes new applications of these techniques to design nanofluidic devices for novel biomolecular sieving and manipulation.

Additionally, as described in Chapter 5, the vertical nanofilter device, using anisotropic etching of (110) Si substrate, needs to be further optimized to achieve the uniform gap size and also decrease in the filter gap size. This device provides 1000-fold or even higher throughput of separation and analysis of biomolecules, compared to the regular

planar nanofluidic filters. The device has been demonstrated for the separation of large DNA molecules. However, the technique should be able to be further used for separation of small DNA molecules, protein, organelles, and carbohydrate, by precisely designing and controlling the appropriate filter size. Furthermore, the devices are not limited for biomolecule size-based sieving but also can be used as biomolecular sieving based on electrostatic interaction with the Debye layer by changing the surface charge density with controlling the buffer ionic strength as well as the zeta potential.

Appendices

Process Flow for Fabrication of PDMS Nanofluidic Channels

General Process: Silicon masters are patterned and etched by standard photolithography and reactive ion etching techniques. PDMS stamps are replicated by replica molding and curing a liquid prepolymer from the silicon masters. Seal PDMS stamps against glass substrate.

Starting Material: clean 6" <100> silicon wafer (single side polished)

Detailed Process Steps:

STEP	FAB	MACHINE	ACTION
------	-----	---------	--------

1. Fabrication of silicon masters

1.1	TRL	Oven	Dehydrate @ 120 °C for 1 hour
1.2	TRL	HMDS	HMDS Coating for 30 min
1.3	TRL	Coater	Spin coating wafer with Image Reversal AZ5214E
1.4	TRL	Oven	Prebake wafer @ 95 °C for 30 min
1.5	TRL	EV1	Expose resist with mask
1.6	TRL	Oven	Postbake wafers @ 95 °C for 25 min
1.7	TRL	EV1	Flood expose 60 sec without mask
1.8	TRL	Photohood	Develop
1.9	ICL	LAM 490B	RIE etch Si
1.10	ICL	Asher	Strip remaining photoresist
1.11	ICL	Pre-metal	Piranha cleaning
1.12	ICL	P-10	Depth measurement

2. Preparation of PDMS

Weight out Sylgard 184 PDMS (Dow Corning, www.dowcorning.com) base and curing agent (10:1). Mix in a cup and degas under vacuum.

To prepare h-PDMS developed by Schmid at al.⁵¹, mix for 5 minutes 30 g of the vinyl PDMS prepolymer (VDT-731, Gelest Corp., www.gelest.com), 15 µL of a platinum catalyst (Platinum divinyltetramethyl-disiloxane complex in xylene, SIP6831.0, Gelest Corp.), and 30.5 µL of a modulator (2,4,6,8-tetramethyltetra-vinylcyclotetra-siloxane, 87927, Sigma-Aldrich, www.sigmaaldrich.org). Stir 9.0 g of a hydrosilane prepolymer (HMS301, Gelest Corp.) into this mixture. Mix completely and degas again. Do not degas for more than half an hour. Keep it in the refrigerator at 4 °C if you need additional

time to get ready. However, the PDMS mixture will be cured after a couple of hours even at the room temperature condition.

3. Micromolding of PDMS

Treat silicon masters with silane to prevent PDMS from sticking on the silicon masters. To do so, place a vial containing a few drops of silane reagent HMDS (tridecafluoro-1,1,2,2-tetrahydro octyl trichlorosilane). Put the wafer in a petri dish, and together with the silane reagent into a vacuum chamber (there is a designated desecrator in EML). Let the silane evaporate under vacuum for at least 30-60 min. Remove the wafer and dispose the vial as chemically contaminated glass.

Weight out PDMS prepolymer and fully mix in a cup. Degas the mixture under vacuum until no bubbles are visible. Pour the mixture slowly on the silicon wafer enclosed by aluminum foil. Avoid bubble. Cure the PDMS in an oven at 65 °C for several hours (2 hours for Sylgard 184 and 24 hours for hard-PDMS). Peel off the PDMS from the master slowly and carefully. Cut the devices out with a blade.

4. Sealing PDMS on glass slides

Punch holes in the device. Clean the PDMS and glass surface with Scotch Tape and then methanol solution. Rinse with DI water and blow dry with nitrogen. Place the PDMS device and glass in the chamber (Plasma Cleaner), close the chamber door, and pump down for 2 min. Turn on the plasma and sustain the plasma with pink color for 30 sec. Turn the plasma off and vent the chamber. Seal the PDMS pieces against the glass substrate.

Fill the reservoirs with DI water or buffer solution. Soak overnight in DI water at 65 °C if necessary to prevent the evaporation.

Process Flow for Fabrication of Nanofluidic Channels on Silicon Substrate

General Process: Nanochannels with various depths are patterned and etched into silicon wafer by photolithography and reactive ion etching techniques. Potassium hydroxide (KOH) etching is used to make access hole through the wafer. A thermal oxide is grown to provide an electrical isolation between silicon substrate and buffer solution. Finally, the silicon wafer is bonded to a Pyrex wafer using anodic bonding technique.

Starting Material: clean 6" <100> silicon wafer (single side polished)

Detailed Process Steps:

Step	Fab	Machine	Action
1	ICL	Coater6	Spin coating wafer with Shipley SPR-1.0
2	TRL	EV1	Expose resist (ALIGNMENT MARK mask)
3	ICL	Coater6	Develop the resist
4	ICL	AME5000	RIE etch silicon for alignment mark (1 μm)
5	ICL	Asher	Strip remaining photoresist
6	ICL	Pre-metal	Piranha cleaning
7	ICL	P-10	Depth measurement
8	ICL	RCA	Standard RCA cleaning
9	ICL	VTR	Low-stress silicon nitride deposition (1000 Å)
10	ICL	Coater6	Spin coating wafer with Shipley SPR-1.0
11	TRL	EV1	Expose resist (ACCESS HOLE mask)
12	ICL	Coater6	Develop the resist
13	ICL	AME5000	RIE etch SiN to open loading holes
14	ICL	Asher	Strip photoresist
15	ICL	TMAH-KOH hood	KOH etching silicon for access holes
16	ICL	Pre-metal	Post-KOH Cleaning
17	ICL	NitrEtch-HotPros	Silicon Nitride Removal
18	ICL	RCA	Standard RCA pre-furnace cleaning
19	ICL	5C-FieldOx	Thermal oxidation (400 nm)
20	TRL	Acidhood	Silicon and Pyrex wafer cleaning
21	TRL	EV501	Anodic bonding
22	ICL	Diesaw	Diesaw Cutting

Process Flow for Fabrication of Nanofluidic Channels on Glass Substrate

General Process: Nanochannels with various depths are patterned and etched into glass wafers by photolithography and wet etching techniques. Access holes can be achieved by mechanical drilling or laser machining. Finally, the glass wafer is bonded to another glass wafer using the thermal fusion bonding technique (glass-glass direct bonding).

Starting Material: clean 6" Pyrex wafer (0.5 mm thick, double side polished, Sensor Prep Services, Inc., IL)

Detailed Process Steps:

Step	Fab	Machine	Action
1	TRL	Acidhood	Piranha cleaning for 10 min
2	TRL	Oven	Dehydrate for at least 1 hour at 120 °C
3	TRL	HMDS	Silane coating
4	TRL	Coater	Resist coating (OCG 825)
5	TRL	Oven	Prebake for 35 min at 95 °C
6	TRL	EV1	Expose resist (2.6 sec)
7	TRL	Photo-wet	Develop in OCG 934 1:1 developer
8	TRL	Oven	Postpake for 30 min at 120 °C
9	TRL	Acidhood	BOE (7:1) etching
10	TRL	Acidhood	Piranha cleaning and surface treatment with 28% ammonium hydroxide
11	EML	Box Furnace	Fusion bonding two glass wafers

References

1. Gravesen, P., Branebjerg, J. & Jensen, O.S. Microfluidics-a review. *J. Micromech. Microeng.* **3**, 168-182 (1993).
2. Lee, S.J. & Lee, S.Y. Micro total analysis system (μ -TAS) in biotechnology. *Appl. Microbiol. Biotechnol.* **64**, 289-299 (2004).
3. Tegenfeldt, J.O. et al. Micro- and nanofluidics for DNA analysis. *Anal. Bioanal. Chem.* **378**, 1678-1692 (2004).
4. Andersson, H. & Berg, A.v.d. Microfabrication and microfluidics for tissue engineering: state of the art and future opportunities. *Lab On a Chip* **4**, 98-103 (2004).
5. Reyes, D.R., Iossifidis, D., Auroux, P.-A. & Manz, A. Micro Total Analysis Systems. 1. Introduction, Theory, and technology. *Analytical Chemistry* **74**, 2623-2636 (2002).
6. Auroux, P.-A., Iossifidis, D., Reyes, D.R. & Manz, A. Micro Total Analysis Systems. 2. Analytical Standard Operations and Applications. *Analytical Chemistry* **74**, 2637-2652 (2004).
7. Sinha, P.M., Valco, G., Sharma, S., Liu, X. & Ferrari, M. Nanoengineered device for drug delivery application. *Nanotechnology* **15**, S585-589 (2004).
8. Han, J. in Introduction to Nanoscale Science and Technology. (ed. J.R. Heflin) (Kluwer, 2004).
9. Chen, Y. & Pépin, A. Nanofabrication: Conventional and nonconventional methods. *Electrophoresis* **22**, 187-207 (2001).
10. Lang, W. silicon microstructuring technology. *Materials Science and Engineering* **R17**, 1-55 (1996).
11. Li, H. & Huck, W.T.S. Polymers in nanotechnology. *Current Opinion in Solid State & Materials Science* **6**, 3-8 (2002).
12. Yu, C., Xu, M., Svec, F. & Fréchet, J.M.J. Preparation of Monolithic Polymers with Controlled Porous Properties for Microfluidic Chip Applications Using photoinitiated Free-Radical Polymerization. *Journal of Polymer Science A* **40**, 755-769 (2002).
13. Ngola, S.M., Fintschenko, Y., Choi, W.-Y. & Shepodd, T.J. Conduct-as-Cast Polymer Monoliths as Separation Media for Capillary Electrochromatography. *Analytical Chemistry* **73**, 849-856 (2001).

14. Throckmorton, D.J., Shepodd, T.J. & Singh, A.K. Electrochromatography in Microchips: Reversed-Phase Separation of Peptides and Amino Acids Using Photopatterned Rigid Polymer Monoliths. *Analytical Chemistry* **74**, 784-789 (2002).
15. Apel, P. Track etching technique in membrane technology. *Radiation Measurements* **34**, 559-566 (2001).
16. Ferain, E. & Legras, R. Track-etch templates designed for micro- and nanofabrication. *Nuclear Instruments and Methods in Physics Research B* **208**, 115-122 (2003).
17. Beck, R.E. & Schultz, J.S. Hindered Diffusion in Microporous Membranes with Known Pore Geometry. *Science* **170**, 1302-1305 (1970).
18. Kuo, T.C., Sloan, L.A., Sweedler, J.V. & Bohn, P.W. Manipulating molecular transport through nanoporous membranes by control of electrokinetic flow: Effect of surface charge density and debye length. *Langmuir* **17** (2001).
19. Nishizawa, M., Menon, V.P. & Martin, C.R. Metal Nanotubule Membranes with Electrochemically Switchable Ion-Transport Selectivity. *Science* **268**, 700 (1995).
20. Jirage, K.B., Hulteen, J.C. & Martin, C.R. Nanotubule-Based Molecular-Filtration Membranes. *Science* **655** (1997).
21. Hulteen, J.C., Jirage, K.B. & Martin, C.R. Introducing Chemical Transport Selectivity into Gold Nanotubule Membranes. *J. Am. Chem. Soc* **120**, 6603 (1998).
22. Che, G., Lakshmi, B.B., Fisher, E.R. & Martin, C.R. Carbon nanotube membranes for electrochemical energy storage and production. *Nature* **393**, 346 (1998).
23. Lee, S.B. & Martin, C.R. pH-Switchable, Ion-Permeable Gold Nanotubule Membrane Based on Chemisorbed Cysteine. *Analytical Chemistry* **73**, 768-775 (2001).
24. Steinle, E.D. et al. Ion Channel Mimetic Micropore and Nanotube Membrane Sensors. *Analytical Chemistry* **74**, 2416-2422 (2002).
25. Han, J. & Craighead, H.G. Separation of Long DNA Molecules in a Microfabricated Entropic Trap Array. *Science* **288**, 1026-1029 (2000).
26. Turner, S.W., Perez, A.M., Lopez, A. & Craighead, H.G. Monolithic nanofluid sieving structures for DNA manipulation. *Journal of Vacuum Science & Technology, B* **16**, 3835-3840 (1998).

27. Austin, R.H., Tegenfeldt, J.O., Cao, H., Chou, S.Y. & Cox, E.C. Scanning the controls: Genomics and Nanotechnology. *IEEE Transactions On Nanotechnology* **1**, 12 (2002).
28. Matthias, S. & Müller, F. Asymmetric pores in a silicon membrane acting as massively parallel brownian ratchets. *Nature* **424**, 53 (2003).
29. Ohji, H., Izuo, S., French, P.J. & Tsutsumi, K. Pillar structures with a sub-micro space fabricated by macroporous-based micromachining. *Sensors and Actuators A* **97-98**, 744-748 (2002).
30. Cao, H. et al. Fabrication of 10 nm enclosed nanofluidic channels. *Applied Physics Letters* **81**, 174-176 (2002).
31. Park, M., Harrison, C., Chaikin, P.M., Register, R.A. & Adamson, D.H. Block copolymer lithography: Periodic arrays of similar to 10(11) holes in 1 square centimeter. *Science* **276**, 1401-1404 (1997).
32. Jeon, S. et al. From the Cover: Fabricating complex three-dimensional nanostructures with high-resolution conformable phase masks. *Proceedings of the National Academy of Sciences of the United States of America* **101**, 12428 (2004).
33. Nykypanchuk, D., Strey, H.H. & Hoagland, D.A. Brownian motion of DNA confined within a two-dimensional array. *Science* **297**, 987 (2002).
34. Saleh, O.A. & Sohn, L.L. An Artificial Nanopore for Molecular Sensing. *Nano Lett.* **3**, 37-38 (2003).
35. Kasianowicz, J., Brandin, E., Branton, D. & Deamer, D. Characterization of individual polynucleotide molecules using a membrane channel. *Proceedings of the National Academy of Sciences of the United States of America* **93**, 13770-13773 (1996).
36. Saleh, O.A. & Sohn, L.L. Quantitative sensing of nanoscale colloids using a microchip coulter counter. *Review of Scientific Instruments* **72**, 4449-4451 (2001).
37. Han, J. & Craighead, H.G. Entropic trapping and sieving of long DNA molecules in a nanofluidic channel. *J. Vac. Sci. Technol. A* **17**, 2142-2147 (1999).
38. Han, J., Turner, S.W. & Craighead, H.G. Entropic trapping and escape of long DNA molecules at submicron size constriction. *Physical Review Letters* **83**, 1688 (1999).
39. Han, J. & Craighead, H.G. Characterization and Optimization of an Entropic Trap for DNA Separation. *Analytical Chemistry* **74**, 394-401 (2002).
40. Fu, J., Mao, P. & Han, J. Gel-Free Size Separation of Biomolecules by a Regular Nanofluidic Molecular Filter Array. *To be submitted* (2005).

41. Davidson, M.G. & Deen, W.M. Hindered Diffusion of Water-Soluble Macromolecules in Membranes. *Macromolecules* **21**, 3474-3481 (1988).
42. Deen, W.M. Hindered Transport of Large Molecules in Liquid-Filled Pores. *AIChE Journal* **33**, 1409-1425 (1987).
43. Kathawalla, I.A. & Anderson, J.L. Pore size effects on diffusion of polystyrene in dilute solution. *Ind. Eng. Chem. Res.* **27**, 866-871 (1988).
44. Kathawalla, I.A., Anderson, J.L. & Lindsey, J.S. Hindered diffusion of porphyrins and short-chain polystyrene in small pores. *Macromolecules* **22**, 1215-1219 (1989).
45. Shao, J. & Baltus, R.E. Hindered Diffusion of Dextran and Polyethylene Glycol in Porous Membranes. *AIChE Journal* **46**, 1149-1156 (2000).
46. Bakajin, O.B. et al. Electrohydrodynamics Stretching of DNA in Confined Environments. *Physical Review Letters* **80**, 2737 (1998).
47. Tegenfeldt, J.O. et al. The dynamics of genomic-length DNA molecules in 100-nm channels. *Proceedings of the National Academy of Sciences of the United States of America* **101**, 10979-10983 (2004).
48. Lyon, W.A. & Nie, S. Confinement and Detection of Single Molecules in Submicrometer channels. *Analytical Chemistry* **69**, 3400-3405 (1997).
49. Foquet, M., Korlach, J., Zipfel, W., Webb, W.W. & Craighead, H.G. DNA fragment sizing by single molecule detection in submicrometer-sized closed fluidic channels. *Analytical Chemistry* **74**, 1415-1422 (2002).
50. Foquet, M., Korlach, J., Zipfel, W.R., Webb, W.W. & Craighead, H.G. Focal Volume Confinement by Submicrometer-sized Fluidic Channels. *Analytical Chemistry* **76**, 1618-1626 (2004).
51. Schmid, H. & Michel, B. Siloxane polymers for high-resolution, high-accuracy soft lithography. *Macromolecules* **33**, 3042-3049 (2000).
52. Quake, S.R. & Scherer, A. From micro- to nanofabrication with soft materials. *Science* **290**, 1536 (2000).
53. Ng, J.M.K., Gitlin, I., Stroock, A.D. & Whitesides, G.M. Components for integrated poly(dimethylsiloxane) microfluidic systems. *Electrophoresis* **23**, 3461-3473 (2002).
54. McDonald, J.C. et al. Fabrication of microfluidic systems in poly(dimethylsiloxane). *Electrophoresis* **21**, 27-40 (2000).

55. McDonald, J.C. & Whitesides, G.M. Poly(dimethylsiloxane) as a material for fabricating microfluidic devices. *Accounts of Chemical Research* **35**, 491 (2002).
56. Xia, Y. & Whitesides, G.M. Soft Lithography. *Annu. Rev. Mater. Sci.* **28**, 153-184 (1998).
57. Unger, M.A., Chou, H.-P., Thorsen, T., Scherer, A. & Quake, S.R. Monolithic Microfabricated Valves and Pumps by Multilayer Soft Lithography. *Science* **288**, 113-116 (2000).
58. Odom, T.W., Love, J.C., Wolfe, D.B., Paul, K.E. & Whitesides, G.M. Improved pattern transfer in soft lithography using composite stamps. *Langmuir* **18**, 5314-5320 (2002).
59. Michel, B. et al. Printing meets lithography: Soft approaches to high-resolution printing. *IBM J. Res & DEV* **45**, 697 (2001).
60. Nas, N.R., Mela, P., Kramer, T., Berenschot, J.W. & Berg, A.v.d. Water plugs in nanochannels under negative pressure. *Proceedings of the MicroTAS 2003 Symposium* (2003).
61. Randall, G.C. & Doyle, P.S. *Proceedings of the National Academy of Sciences of the United States of America* **Submitted** (2004).
62. Chen, Y.-L. et al. Conformation and dynamics of single DNA molecules in parallel-plate slit microchannels. *Physical Review E* **70**, 060901 (2004).
63. Eijkel, J.C.T., Bomer, J.G. & Berg, A.v.d. Osmosis and pervaporation observed in polyimide sub-micro channels. *Proceedings of the MicroTAS 2004 Symposium 1*, 405 (2004).
64. Han, J. (Cornell University, Ithaca, NY; 2001).
65. Wallis, G. & Pomerantz, D.I. Field Assisted Glass-Metal Sealing. *J. Appl. Phys.* **40**, 3946 (1969).
66. Chavan, A.V. & Wise, K.D. A monolithic fully-integrated vacuum-sealed CMOS pressure sensor. *IEEE Trans. Electron. Devices* **ED49**, 164-169 (2002).
67. Acero, M.C. et al. Design of a modular micropump based on anodic bonding. *J. Micromech. Microeng.* **7**, 179-182 (1997).
68. Schjølberg-Henriksen, K., Jensen, G.U., Hanneborg, A. & Jakobsen, H. Anodic bonding for monolithically integrated MEMS. *Sensors and Actuators A* **114**, 332-339 (2004).
69. Madou, M. Fundamentals of microfabrication. (CRC Press, Boca Raton, Florida; 1997).

70. Li, G.Y. & Wang, L. Influence of bonding parameters on electrostatic force in anodic wafer bonding. *Thin Solid Films* **462-463**, 334-338 (2004).
71. Rogers, T. & Kowal, J. Selection of glass, anodic bonding conditions and material compatibility for silicon-glass capacitive sensors. *Sensors and Actuators A* **46-47**, 113-120 (1995).
72. Anthony, T.R. Anodic bonding of imperfect surfaces. *J. Appl. Phys.* **54**, 2419-2428 (1983).
73. Lee, T.M.H., Lee, D.H.Y., Liaw, C.Y.N., Lao, A.I.K. & Hsing, I.-M. Detailed characterization of anodic bonding process between glass and thin-film coated silicon substrates. *Sensors and Actuators A* **86**, 103-107 (2000).
74. Wei, J., Wang, Z.P., Xie, H. & Lan, N.F. Role of bonding temperature and voltage in silicon-to-glass anodic bonding. *IEEE Electronics Packaging Technology Conference*, 85 (2002).
75. Shih, W.-P., Hui, C.-Y. & Tien, N.C. Collapse of microchannels during anodic bonding: Theory and experiments. *J. Appl. Phys.* **95**, 2800-2808 (2004).
76. Turner, S.W., Perez, A.M., Lopez, A. & Craighead, H.G. Monolithic nanofluid sieving structures for DNA manipulation. *Journal of Vacuum Science & Technology, B: Microelectronics Processing and Phenomena* **16**, 3835-3840 (1998).
77. Plaza, J.A., Esteve, J. & Lora-Tamayo, E. Effect of silicon oxide, silicon nitride and polysilicon layers on the electrostatic pressure during anodic bonding. *Sensors and Actuators A* **67**, 181-184 (1998).
78. Gösele, U. et al. Wafer bonding for microsystems technologies. *Sensors and Actuators A* **74**, 161-168 (1999).
79. Raleigh, L. A study of glass surfaces in optical contact. *Proc. Phys. Soc. A* **156**, 326-349 (1936).
80. Gösele, U. & Tong, Q.-Y. Semiconductor Wafer Bonding. *Annu. Rev. Mater. Sci.* **28**, 215-241 (1998).
81. Min, H.-S., Joo, Y.-C. & Song, O.-S. Effects of Wafer Cleaning and Annealing on glass/silicon wafer direct bonding. *Transactions of the ASME* **126**, 120-123 (2004).
82. Jia, Z.-j., Fang, Q. & Fang, Z.-L. Bonding of Glass Microfluidic Chips at Room Temperatures. *Analytical Chemistry* **76**, 5597 (2004).

83. Wang, H.Y., Foote, R.S., Jacobson, S.C., Schneibel, J.H. & Ramsey, J.M. Low temperature bonding for microfabrication of chemical analysis devices. *Sensors and Actuators B* **45**, 199-207 (1997).
84. Huang, Z., Sanders, J.C., Dunsmor, C., Ahmadzadeh, H. & Landers, J.P. A method for UV-bonding in the fabrication of glass electrophoretic microchips. *Electrophoresis* **22**, 3924-3929 (2001).
85. Sayah, A., Solignac, D., Cueni, T. & Gijs, M.A.M. Development of novel low temperature bonding technologies for microchip chemical analysis applications. *Sensors and Actuators B* **84**, 103-108 (2000).
86. Chiem, N., Lockyear-Shultz, L., Andersson, P., Skinner, C. & Harrison, D.J. Room temperature bonding of micromachined glass devices for capillary electrophoresis. *Sensors and Actuators B* **63**, 147-152 (2000).
87. Lin, C.-H., Lee, G.-B., Lin, Y.-H. & Chang, G.-L. A fast prototyping process for fabrication of microfluidic systems on soda-lime glass. *J. Micromech. Microeng.* **11**, 726-732 (2001).
88. Fan, Z.H. & Harrison, D.J. Micromachining of Capillary Electrophoresis Injectors and Separators on Glass Chips and Evaluation of Flow at Capillary Intersections. *Analytical Chemistry* **66**, 177-184 (1994).
89. Vossen, J.L. & Kern, W. Thin Film Processes. (Academic Press, New York; 1978).
90. Wang, Y.-C. & Han, J. **to be submitted** (2004).
91. Kendall, D.L. On etching very narrow grooves in silicon. *Applied Physics Letters* **26**, 195-198 (1975).
92. Uenishi, Y., Tsugai, M. & Mehregany, M. Micro-opto-mechanical devices fabricated by anisotropic etching of (110) silicon. *J. Micromech. Microeng.* **5**, 305-312 (1995).
93. Hölke, A. & Henderson, H.T. Ultra-deep anisotropic etching of (110) silicon. *J. Micromech. Microeng.* **9**, 51-57 (1999).
94. Ciarlo, D.R. A latching accelerometer fabricated by the anisotropic etching of (110) oriented silicon wafers. *J. Micromech. Microeng.* **2**, 10-13 (1992).
95. Matthias, S. & Müller, F. Asymmetric pores in a silicon membrane acting as massively parallel brownian ratchets. *Nature* **424**, 53-57 (2003).
96. Jeon, S. et al. From the Cover: Fabricating complex three-dimensional nanostructures with high-resolution conformable phase masks. *PNAS* **101**, 12428-12433 (2004).

97. Jiang, H., Yoo, K., Yeh, J.-L.A., Li, Z. & Tien, N.C. Fabrication of thick silicon dioxide sacrificial and isolation blocks in a silicon substrate. *J. Micromech. Microeng.* **12**, 87-95 (2002).
98. Lehmann, V. & Föll, H. Formation mechanism and properties of electrochemically etched trenches in n-type silicon. *J. Electrochem. Soc.* **137**, 653-658 (1990).
99. Barillaro, G., Nannini, A. & Piotta, M. Electrochemical etching in HF solution for silicon micromachining. *Sensors and Actuators A* **102**, 195-201 (2002).
100. Lehmann, V. & Grüning, U. The limits of macropore array fabrication. *Thin Solid Films* **297**, 13-17 (1997).
101. Smith, D.E., Perkins, T.T. & Chu, S. Dynamical scaling of DNA diffusion coefficients. *Macromolecules* **29**, 1372-1373 (1996).
102. Dittrich, P.S. & Schwille, P. Spatial Two-photon Fluorescence Cross-correlation Spectroscopy for Controlling Molecular Transport in Microfluidic Structures. *Analytical Chemistry* **74**, 4472-4479 (2002).
103. Haustein, E. & Schwille, P. Ultrasensitive investigations of biological systems by fluorescence correlation spectroscopy. *Methods* **29**, 153-166 (2003).